Menon, K. and Mittal, R., 2019. Flow physics and dynamics of flow-induced pitch oscillations of an airfoil. Journal of Fluid Mechanics, 877, pp.582-613
DOI: https://doi.org/10.1017/jfm.2019.627

Flow physics and dynamics of flow-induced pitch oscillations of an airfoil

Karthik Menon[1] and Rajat Mittal[1]†

[1]Department of Mechanical Engineering, Johns Hopkins University, Baltimore, MD 21218, USA

(Received xx; revised xx; accepted xx)

We conduct a computational study of flow-induced pitch oscillations of a rigid airfoil at a chord-based Reynolds number of 1000. A sharp-interface immersed boundary method is used to simulate two-dimensional incompressible flow, and this is coupled with the equations for a rigid foil supported at the elastic axis with a linear torsional spring. We explore the effect of spring stiffness, equilibrium angle-of-attack and elastic-axis location on the onset of flutter, and the analysis of the simulation data provides insights into the time-scales and mechanisms that drive the onset and dynamics of flutter. The dynamics of this configuration includes complex phenomena such as bifurcations, non-monotonic saturation amplitudes, hysteresis and non-stationary limit-cycle oscillations. We show the utility of "maps" of energy exchange between the flow and the airfoil system, as a way to understand, and even predict this complex behavior.

1. Introduction

Aeroelastic wing flutter has attracted scientific attention for many decades due to its importance in the air-vehicle design and performance. More recently, there has been renewed interest in this phenomenon due to the drive towards higher thrust-to-weight ratios in aircrafts that use lighter (and therefore more flexible) materials. Unconventional air-vehicles such as high-altitude and high aspect-ratio aircrafts tend to be more susceptible to aeroelastic effects (Patil & Hodges 2004). Finally, the advent of micro- and unmanned air-vehicles has also spurred research in aeroelastic phenomena, particularly at lower Reynolds numbers (Shyy *et al.* 2007). It is noted that while most of these applications are aimed at suppressing flutter, there is also interest in enhancing flutter as a way to harness energy from flows (Peng & Zhu 2009; Onoue *et al.* 2015). A comprehensive review of efforts in this direction was undertaken by Young *et al.* (2014).

The classical work of Theodorsen (1935) was amongst the earliest attempts at modelling pitching airfoils and their associated unsteady loading. Due to the fact that it is based on first principles and very simple assumptions, this work continues to be used as the basis for new models (Brunton & Rowley 2009). The unsteady aerodynamics of pitching airfoils and dynamic stall is characterized by the generation and shedding of strong leading-edge vortices, accompanied by large regions of separating and reattaching flow on the suction surface of the airfoil (Ericsson & Reding 1988; Eldredge & Jones 2019). This leads to dynamically varying loading conditions and complicated flow fields over the airfoil. The need to better understand this non-linear phenomenon has motivated research into models for unsteady airfoils that go beyond classical theories (McCroskey 1982). In one such detailed study, Lee & Gerontakos (2004) characterized the points of separation, reattachment, and transition on the surface of a pitching airfoil, and showed

† Email address for correspondence: mittal@jhu.edu

the importance of the pitching frequency in these boundary layer events. Other recent studies have investigated the effect of various other parameters related to the pitch frequency, airfoil shape, freestream conditions, etc. (Akbari & Price 2003; Amiralaei *et al.* 2010; Ashraf *et al.* 2011; Gharali & Johnson 2013).

While studies of dynamic stall have predominantly focused on prescribed kinematics, there has also been work to understand the flow-induced response of oscillating airfoils. Poirel *et al.* used a combination of experimental (Poirel *et al.* 2008) and computational (Poirel *et al.* 2011) studies to investigate the effect of flow speed and free-stream turbulence, among other factors, on small amplitude flow-induced pitching oscillations of an airfoil at transitional Reynolds numbers ($Re_c \sim 10^4 - 10^5$). A key finding from their work was that laminar separation is a driving factor for triggering the oscillations in this range of Reynolds number. They also proposed that the oscillations are not dictated by the Karman shedding that was observed, but instead by the separated laminar shear layer. In another study using numerical simulations, Ducoin & Young (2013) studied the stability of a flexible hydrofoil section to bend and twist deformations. Specifically, they investigated the influence of laminar to turbulent transition and viscous effects on the location of the center-of-pressure with respect to the elastic-axis as well as the static divergence velocity.

Significant interest in such studies involving flow-induced oscillations has stemmed from efforts to understand the energy-harvesting potential of aeroelastic flutter, and characterize parametric regimes that allow the growth of flutter instabilites. In one such study, Peng & Zhu (2009) studied the energy-harvesting capability of a flow-induced pitching and heaving airfoil at $Re = 1000$. They proposed the use of linear stability analysis with the dynamical equation of the oscillating airfoil, where the model of Theodorsen (1935) was used to close the forcing term in the equation. They were able to propose parameter ranges for the stiffness and damping of the structure within which flow-induced oscillations are possible. They also studied various oscillatory response regimes as functions of the structural stiffness and damping. Other researchers (Orchini *et al.* 2013; Olivieri *et al.* 2017) have also used similar ideas based on linear stability analysis to predict the condition for the onset of self-sustained flutter. Interestingly, they demonstrate that the onset condition is related to a resonance between the natural frequency of the elastic structure and an aerodynamic frequency, which they estimate as the frequency associated with the pitching moment on a wing that is allowed to pitch freely. This idea of a resonance-based onset condition is derived from the earlier work of Argentina & Mahadevan (2005). Indeed, in the current work we find a related onset condition for purely pitching oscillations, via a system identification approach, and also explore its dependence on the equilibrium angle-of-attack of the airfoil.

Experimentally, Dimitriadis & Li (2009) performed an investigation at a higher Reynolds number of a two-degree-of freedom airfoil that was allowed to perform flow-induced pitch and heave oscillations. They showed the occurrence of various bifurcations as a function of freestream velocity. These were seen to produce symmetric, antisymmetric, as well as hysteretic pitching oscillations depending on the freestream velocity. Further, the recent development of so-called cyber-physical experimental facilities by various research groups (Morse & Williamson 2009; Onoue *et al.* 2015) has led to an increase in the number of experimental studies on flow-induced oscillations. In one such study, Onoue & Breuer (2018) used a flow-induced pitching flat plate to analyze the generation and shedding of the LEV, along with the resultant torques. In another study, Onoue *et al.* (2015) were able to use this experimental system to map out the bifurcation diagram for the system over a large range of oscillation amplitudes. They

compared their results against the classical Theodorsen theory, and also demonstrated the potential for energy harvesting from such systems.

These studies show the presence of a rich variety of response behaviours and bifurcations that characterize the flow-induced pitching of airfoils. However, there is very little knowledge of the dynamics of this problem at low Reynolds numbers that are inaccessible to most experiments. It is well-known that the low-Reynolds number behaviour of airfoils is markedly different from that at high Reynolds number. Mueller & DeLaurier (2003) attributed this to the laminar state of the boundary layer, due to which separated flow fails to reattach, causing very different lift and drag behaviour in this regime. This was also shown to be a factor in driving pitch oscillations of an airfoil by Poirel *et al.* (2008). In addition, the vortex shedding behaviour and associated timescales are known to vary with Reynolds number, especially at the low range of Reynolds numbers. We will show that this timescale is an important factor in the flutter response.

The vastness of the space of parameters and responses that have been shown by previous studies indicate the difficulty of exploring this problem within the constraints of experiments. Historical efforts to model aeroelastic flutter have mainly relied on simplified, or potential-flow based models (Dowell 1966; Jumper *et al.* 1989; Holmes & Marsden 1978; Jones & Platzer 1996). These models are often inadequate to capture the entire range of dynamics in this highly non-linear problem. The use of reduced-order models have also allowed for accurate, computationally economical modelling of aeroelastic flutter (Dowell & Hall 2001; Hall 1994; Ramesh *et al.* 2015). However, the accuracy of reduced-order models can benefit from a detailed knowledge of the flow physics and dynamics of flutter. This further motivates the use high-fidelity computational modelling to study aeroelastic flutter.

Here we report on simulations of the full, two-dimensional incompressible Navier-Stokes equations, which are coupled with a elastically supported NACA0015 airfoil that is allowed to oscillate in pitch. The simulations are performed using a sharp-interface immersed boundary method that allows us to model very large amplitude oscillations in a robust manner. Due to the current lack of data concerning this problem in the existing literature, especially from computational models, one aim of this study is to perform broad parameter sweeps to describe the flow physics governing the onset of flutter, as well as the amplitude and frequency response. We show that this provides fundamental insight into the onset of large amplitude flutter, along with a physically relevant flow time-scale. We also discuss the mechanism that determines the frequency of flutter, and demonstrate the (apparent) difficulty in understanding the amplitude response in some cases.

A second focus of this study is the prediction of the flutter amplitude of flow-induced oscillations using data from forced oscillations. The relationship between forced and flow-induced vibrations - and ultimately the prediction of flow-induced oscillations from data on forced oscillations is a question that has been raised multiple times in studies of vortex-induced vibrations of bluff bodies (Staubli 1983; Hover *et al.* 1998; Morse & Williamson 2006; Leontini *et al.* 2006; Sarpkaya 1978). Morse & Williamson (2009), and Kumar *et al.* (2016) showed, by using the energy extracted by the oscillator from the fluid, that they can be related under carefully matched conditions. Morse & Williamson (2009) also showed the ability to explain various features of the response branches seen in the case of heaving cylinders, based on the energy transfer.

In the context of pitching airfoils, Bhat & Govardhan (2013) used forced oscillations in their experiments to calculate the energy transfer between the fluid and the airfoil, and demarcate flutter boundaries based on this information. In the current study, we extend this idea to explore flutter bifurcations and predict the highly complex response

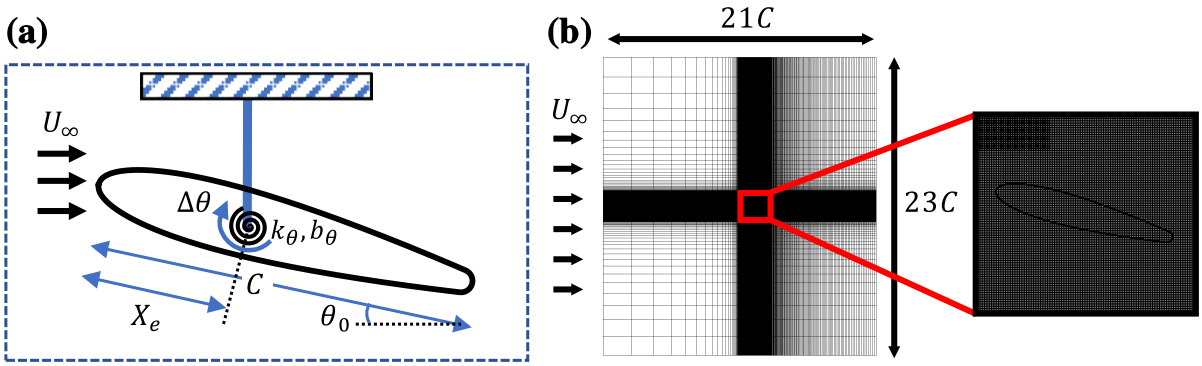

FIGURE 1. (a) Schematic of the aeroelastic system used in this study; (b) Computational domain and close-up of the Cartesian computational grid.

of aeroelastically fluttering airfoils. This is a particularly valuable tool in this context because the flow as well as the dynamical response is significantly more complicated than that observed in the case of transverse oscillations of bluff bodies. This added complexity is in part due to the presence of multiple interacting shear layers (leading and trailing edge), as well as the introduction of additional free parameters such as the location of the elastic axis and the equilibrium angle of attack.

In this study, we show that it is indeed possible to relate the results of forced-oscillations to flow-induced oscillations in the case of pitching airfoils too. We demonstrate a method to analyze pitching oscillations of an airfoil using the energy extracted from the fluid during forced oscillations under similar conditions. This enables us to understand highly complex and counter-intuitive amplitude responses and flutter bifurcations. Further, we also demonstrate the use of forced oscillations and the associated energy transfer to predict transient as well as stationary state amplitude response in flow-induced oscillations.

2. Computational model and numerical method

2.1. *Problem setup*

The two-dimensional computational model in the current study employs a rigid NACA0015 airfoil with a slightly rounded trailing-edge, immersed in an incompressible fluid with freestream velocity U_∞. The slight rounding of the trailing-edge ensures that the flow is well-resolved around it, and we have verified that this has no significant effect on the aerodynamic characteristics and forces on the airfoil. The governing incompressible Navier-Stokes equations expressed in the dimensionless form as follows

$$\frac{\partial \vec{u}}{\partial t} + \vec{u} \cdot \vec{\nabla}\vec{u} = -\vec{\nabla}p + \frac{1}{Re}\nabla^2 u \tag{2.1}$$

where $Re = \rho U_\infty C/\mu$ is the chord-based Reynolds number. The torsional elasticity of the airfoil is modelled using a linear torsional spring with spring constant k and damping coefficient b, attached to the rigid airfoil at a prescribed chordwise location (X_e), which we refer to as the elastic axis (normalized location denoted as $X_e^* = X_e/C$). The equilibrium angular position of the spring is denoted by angle θ_0. A schematic of this setup is shown in figure 1.

The structural system is governed by the equation for a forced spring-mass-damper oscillator. The equation is scaled by the characteristic variables used for the flow (length: C; time: c/U_∞), and the resulting non-dimensionalized equation governing the dynamics

in pitch of the airfoil is given by

$$I^*\ddot{\theta} + b^*\dot{\theta} + k^*(\theta - \theta_0) = C_M \tag{2.2}$$

where $C_M = M/(0.5\rho U_\infty^2 C^3)$ is the coefficient of aerodynamic pitching moment, and $I^* = 2I/(\rho C^4)$, $b^* = 2b/(\rho U_\infty C^3)$, $k^* = 2k/(\rho U_\infty^2 C^2)$ are the dimensionless moment-of-inertia, damping, and spring stiffness respectively. Here, C_M and I^* are calculated with respect to X_e^*. The spring stiffness is commonly expressed in terms of a reduced velocity, $U^* = U_\infty/f_s C$ where $f_s = \frac{1}{2\pi}\sqrt{\frac{k}{I}}$ is the natural frequency of the spring. In essence, U^* is a ratio of the natural time-scale of the elastic system to the convective time-scale of the flow. However, as we will show, the choice of fluid time-scale has significant implications for the dynamics of the system.

Thus, even this highly simplified configuration has six governing parameters (Re, X_e^*, I^*, b^*, U^*, θ_0) and this is indicative of the inherent complexity of this configuration. In the current study, we fix the values of Re and I^* to 1000 and 4.1 respectively and explore the effect of the other four parameters. The Reynolds number chosen is high enough so as to generate robust vortex shedding phenomenon, which drives flutter, but is also low enough so as to allow resolved simulations at a reasonable computational expense. The choice of the moment-of-inertia about the elastic axis corresponds to a solid-to-fluid density ratio of ≈ 120. While the effect of varying I^* in this system could be of significant engineering interest, we choose to use a fixed value throughout this study to reduce the number of independent parameters. However, it must be noted that varying I^* is equivalent to changing the natural frequency as $f_s \sim 1/\sqrt{I^*}$, which is an important parameter in this study.

The current study addresses structurally damped as well as undamped systems with damping being defined by $\zeta^* = b/b_{cr}$ where $b_{cr} = 2\sqrt{kI}$, is the critical damping for the harmonic oscillator. For the undamped system $\zeta^* = 0$ and for the damped system we prescribe $\zeta^* = 0.15$ where this lightly damped structure enables us to understand the effect of damping without overly damping the pitch oscillations. The remaining two parameters, the elastic axis (X_e^*) and the spring stiffness (U^*), are a particular focus of the current study. For X_e^*, we use three values - $X_e^* = 0.50$, 0.33 and 0.25 - and we will show that these generate very significant variations in the pitch response. The final parameter U^* represents the spring stiffness (a larger U^* corresponds to a softer spring) and this parameter is varied from about 2 to 13.

2.2. *Numerical method*

We simulate the coupled fluid-structure system using the sharp-interface immersed boundary method based solver "ViCar3D" described in Mittal *et al.* (2008) and Seo & Mittal (2011). This allows us to preserve sharp interfaces along the surface of our geometry using a body-non-conformal Cartesian grid. This is particularly useful in fluid-structure interaction studies as it allows us to simulate a variety of shapes as well large-amplitude motions on simple, non-adaptive Cartesian grids. In particular, this approach has the advantage of not being constrained by highly deformed grid cells or the need to periodically recompute the grid during high-amplitude motions (Mittal & Iaccarino 2005). The fluid equations are solved using a second-order fractional-step method, and the pressure Poisson equation is solved using the geometric multigrid method. Second-order finite differences are used for all spatial derivatives, and the time-integration is performed using a second order Adams-Bashforth method. ViCar3D employs a boundary imposition scheme that is second-order accurate and consequently, models surface quantities such as pressure and shear with high-fidelity (Mittal *et al.* 2008). ViCar3D has been validated

and verified extensively for a variety of stationary and moving boundary problems in earlier papers (Ghias *et al.* 2007; Mittal *et al.* 2008; Seo & Mittal 2011), as well as during the current study (see appendix B).

The fluid-structure coupling employs a loosely-coupled approach wherein the flow and dynamical equation are solved sequentially. The aerodynamic forces/moments are calculated on the Lagrangian marker points on the surface of the solid body, and passed on to the solid dynamical equation (equation 2.2). The angular velocity predicted from this equation is subsequently imposed on the marker points. The aeroelastic system is immersed in a large $21C \times 23C$ computational domain, where the airfoil is placed 10 chord-lengths from the downstream boundary, and the isotropic grid resolution around the solid body corresponds to about 125 points along the chord. The grid is stretched in all directions away from the rectangular region that surrounds the foil and the near-wake resulting in a baseline grid of 384×320 points. A Dirichlet velocity boundary condition is used at the inlet boundary of the domain, and zero-gradient Neumann conditions are specified at all other boundaries. Grid refinement studies described in the appendix B confirm that the results on this grid are well converged.

For all the cases, simulated here, we initialize the airfoil at its equilibrium angle θ_0, with zero initial angular velocity. The constant freestream flow is then imposed and the dynamics allowed to evolve until the system reaches a stationary state. For the cases simulated here, it takes between $O(20)$ and $O(200)$ oscillation cycles before this stationary state is achieved. Average quantities are computed after the stationary state is reached.

3. Results

3.1. *Qualitative Features*

We begin our discussion of the aeroelastic response of this system by providing an overview of one representative case for which, $U^* = 6.6$, $X_e^* = 0.5$, $\zeta = 0.15$, and $\theta_0 = 15^\circ$. This case develops fairly large amplitude pitch oscillations ($A_\theta \approx 45^\circ$) and serves to demonstrate the various flow structures and non-linear interactions that drive the pitching of the airfoil. In figure 2 are snapshots of the flow over the course of one oscillation cycle. The time series for the coefficients of moment (C_M) and lift (C_L) corresponding to the same oscillation cycle are shown in figure 2(b) and 2(c).

As the airfoil pitches up at the start of the cycle, in figure 2(1), we see that there is initially a monotonic increase in C_M and C_L. This is related to the fact that the shear layer on the suction side is stabilized by the motion of the airfoil until angles of attack well past the static stall angle (which for this airfoil, at this Reynolds number, is about 20 degrees). This stabilization of the boundary layer over a pitching airfoil was also reported by Lee & Gerontakos (2004). However, this pitch-up motion destabilizes the pressure-side boundary layer. As a result, there is a roll-up of the leading-edge shear layer on the pressure side, and a vortex convects downstream along the pressure side, as seen in figure 2(2). As this vortex moves past the trailing edge, there is a sudden drop in C_M and a slight rise in C_L. However, the airfoil continues to rotate on account of inertia, until it reaches its maximum pitch position. Close to the end of this motion, the LEV begins to grow, along with the shedding of a trail of smaller vortices from the trailing edge, seen in figure 2(3). A similar observation was made by Onoue & Breuer (2016), who attributed the origin of this to a Kelvin-Helmholtz-like instability in the trailing-edge shear layer. This is accompanied by a sharp loss in C_L at the end of the pitch-up motion.

As the airfoil begins pitching down, there is an initial monotonic decrease in C_M and C_L that appears to mirror the initial stage of the pitch-up motion. We also see

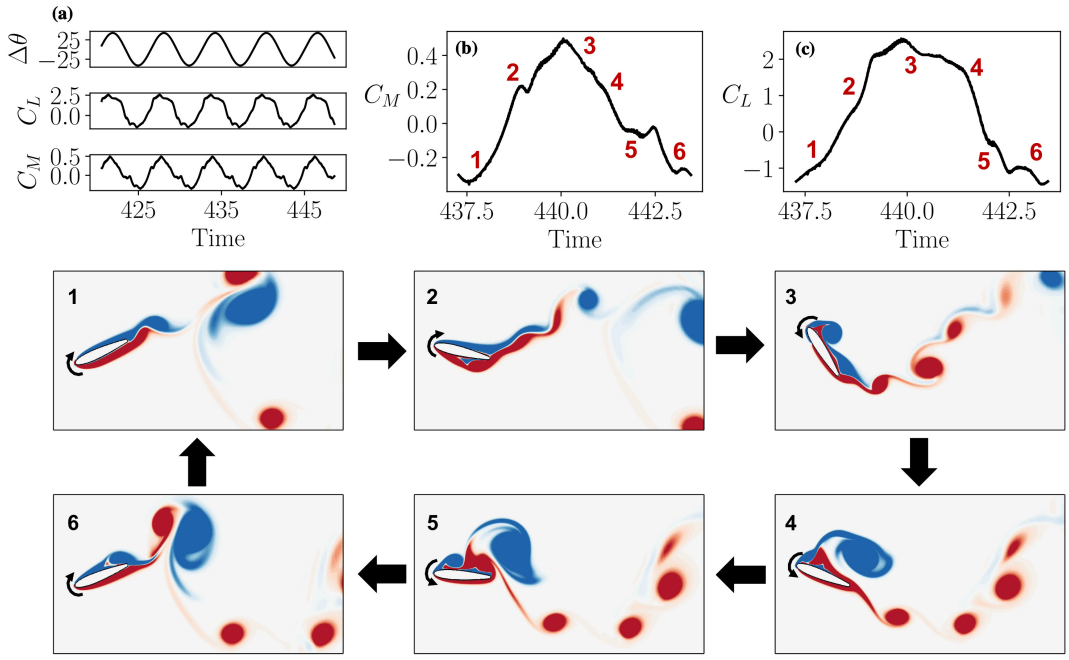

FIGURE 2. A representative case of flow-induced pitching oscillations with $U^* = 6.6$, $X_e^* = 0.50$, $\theta_0 = 15^\circ$ and $\zeta = 0.15$; The top panel shows time series plots of (a) pitch deflection ($\Delta\theta$), coefficient of moment (C_M), and coefficient of lift (C_L); (b) coefficient of moment during one cycle of oscillation (corresponding to the cycle shown in the snapshots); (c) coefficient of lift during the cycle corresponding to the snapshots; (1-6) Snapshots of the flow-field coloured by contours of z-vorticity.

that the presence of the LEV over the suction surface in figure 2(4) influences the rate of this decrease. This pitch-down motion destabilizes the suction-side shear layer, and leads to the shedding of a second, smaller LEV in figure 2(5). At the same time, a trailing-edge vortex is generated and shed, and this vortex seems to be influenced by the strong entrainment due to the LEV convecting past the trailing edge. This effect is seen in the majority of cases simulated. The simultaneous presence of this TEV and LEV near the suction side trailing edge causes a strong uptick in C_M, which causes it go over its pitch-up value. This interesting effect leads to a counter-clockwise loop in the C_M hysteresis curve(not shown here), which has implications for energy harvesting applications. Subsequently, C_M continues to decrease and C_L plateaus as the second LEV convects over the suction side in figure 2(6). The movement of this LEV past the trailing edge then produces a drop in C_L and a brief increase in C_M.

This representative case shows that the airfoil experiences strongly non-linear loading over the course of an oscillation cycle. The occurrence of limit-cycle oscillations, which we see in spite of a linear structural model, is only possible in the presence of such non-linearities in the system. Hence, this supports the notion that large scale flow separation is the primary cause of limit cycle oscillations in this system. Further, there is a complex interaction between the leading and trailing edge shear layers, as well as the generation and shedding of multiple LEVs. The timing and position of these flow structures plays a crucial role in the dynamics of pitch oscillations, and this analysis of some representative flow interactions forms a starting point of our discussion.

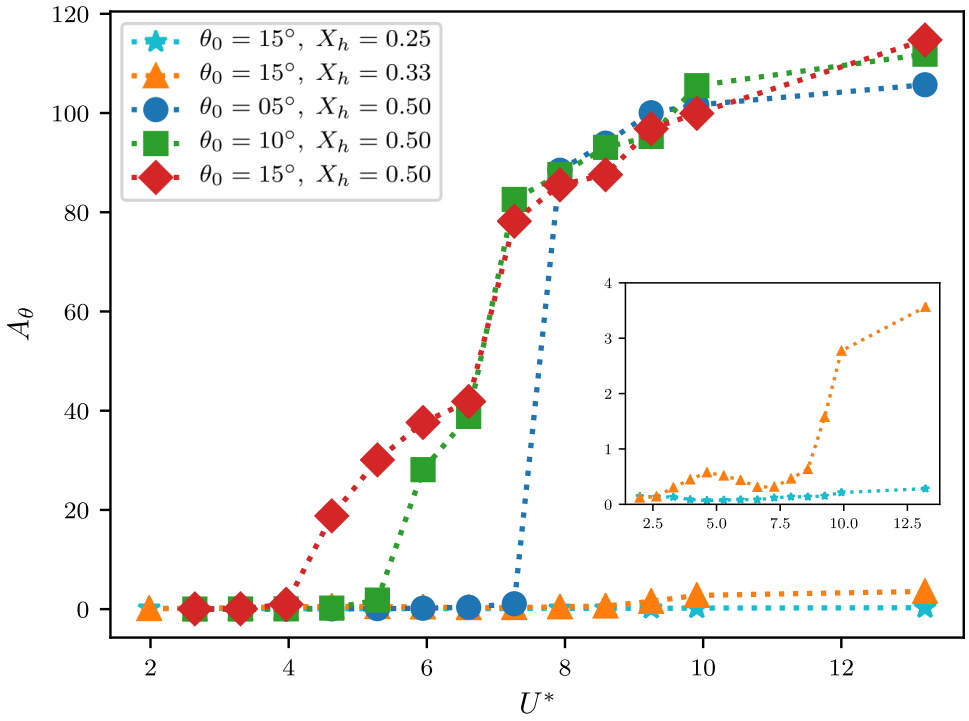

FIGURE 3. Maximum pitch deflection, A_θ, as a function of U^* for different values of θ_0 and X_e^*. For all cases shown here, $\zeta = 0.15$. The inset shows a zoom-in for $X_e^* = 0.25$ and $X_e^* = 0.33$.

3.2. *Effect of Key Parameters on Flutter Response*

The overall effect of spring stiffness (U^*), equilibrium angle-of-attack, and elastic axis location on the flutter amplitude is discussed in this section. In figure 3, we show the maximum stationary-state pitch deflection from the equilibrium (denoted as A_θ), as a function of U^* for the case with nonzero structural damping. This is plotted for three different equilibrium pitch angles, $\theta_0 = 5°, 10°, 15°$, and three different locations of the elastic axis, $X_e^* = 0.25, 0.33, 0.50$. It is immediately clear that this system can show very large pitch deflections, going as high as 100°, for the case of $X_e^* = 0.50$. However, the pitch deflections for $X_e^* = 0.25$ and 0.33 are very small for the same range of U^*. Further, while the response for $X_e^* = 0.50$ increases monotonically with U^*, the response for $X_e^* = 0.33$ shows a non-monotonic trend (shown in the inset). These observations suggest that the amplitude response of this system is very sensitive to the location of the elastic axis, and this issue is investigated further in sections 3.5 and 4. The lack of response at $X_e^* = 0.25$ is not surprising since the aerodynamic center of most airfoils is in the vicinity of 25% chord (Abbott & Von Doenhoff 1959) and placing the elastic-axis at or near this location should diminish pitch-instability.

We now focus on the large amplitude flutter observed for the $X_e^* = 0.50$ cases. We see that the onset of these large amplitude oscillations occurs at a different (critical) U^* (referred to as U_c^*) for each value of θ_0. Lower θ_0 require softer springs (or higher U^*) in order to initiate deflections. Interestingly, A_θ for different values of θ_0 approach each other for very large pitch deflections indicating that the system loses memory of the equilibrium condition for very soft springs. As a result of this, and the fact that the bifurcation is delayed for lower θ_0, the onset of large amplitude oscillations is more abrupt as we go to lower θ_0, i.e., the curve for $\theta_0 = 5°$ has a larger slope than that for $\theta_0 = 10°$. This points to the possibility of a bifurcation that has an increasingly subcritical nature as θ_0 is reduced. This is in agreement with Onoue *et al.* (2015) and Dimitriadis & Li

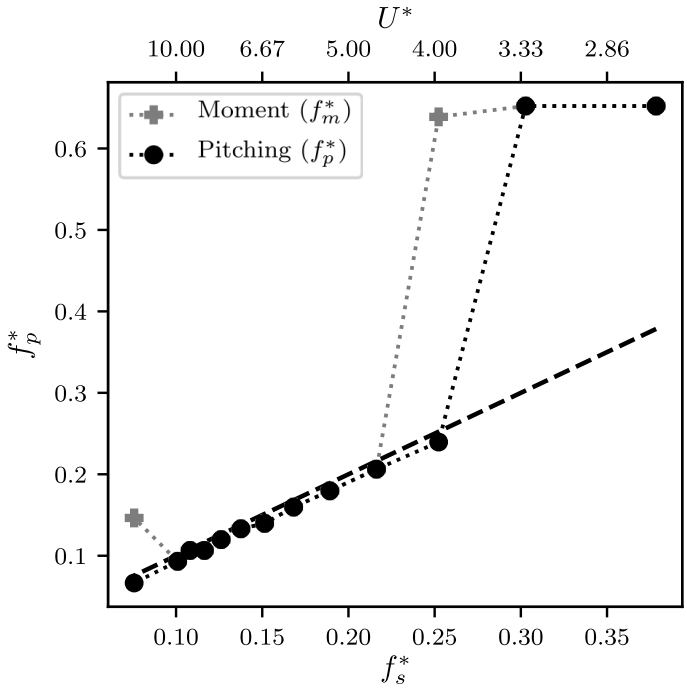

FIGURE 4. Pitch and moment frequency response as a function of U^* for $\theta_0 = 15°$, $X_e^* = 0.50$ and $\zeta = 0.15$. The dashed line shows the natural frequency.

(2009) who observed a subcritical bifurcation for $\theta_0 = 0°$. It must be noted here that unlike the case of $\theta_0 = 0°$, our system shows small, but nonzero values of A_θ even for very low U^*. These oscillations are associated with the oscillatory pitch-moments induced by Karman vortex shedding. However, we will show the presence of subcritical behaviour even in the case of $\theta_0 = 15°$ later in this paper.

3.3. *Frequency response*

In the previous section, we showed that the system loses memory of the equilibrium condition (θ_0) for large flutter amplitudes. Considering this, we will conduct a detailed analysis for one case, namely $\theta_0 = 15°$. In figure 4 we show the pitch oscillation frequency ($f_p^* = f_p C/U$) compared with the frequency of moment oscillations ($f_m^* = f_m C/U$) for the structurally damped case with $\theta_0 = 15°$ and $\zeta = 0.15$. This is plotted with respect to the dimensionless natural frequency f_s^* as well as $U^* = 1/f_s^*$. The dashed line in figure 4 denotes the synchronization condition, i.e., the condition where the pitch frequency equals the natural frequency of the system. We see that for low (high) values of U^* (f_s^*), the pitch as well as moment oscillations occur at a constant, high frequency. On increasing U^*, there is a sudden drop in frequency which corresponds to the same U^* value at which the bifurcation to large-amplitude pitch oscillation occurs - following which, the pitch oscillations synchronize with the natural frequency for higher (lower) values of U^* (f_s^*). Hence, there are three distinct frequency response regimes that occur for increasing (decreasing) U^* (f_s^*): constant, high frequency pitch and moment, followed by the moment de-tuning from the pitch at the bifurcation point, and finally the moment and pitch oscillations synchronizing with the natural frequency of the system.

It is instructive to examine the flow quantities during these distinct regimes to understand how the flow drives the dynamics of flutter, and vice-versa. In figure 5 we show plots of the pitch and moment time series, along with a snapshot of the flow, for three representative cases very close to the bifurcation point. For $U^* = 3.3$, which corresponds

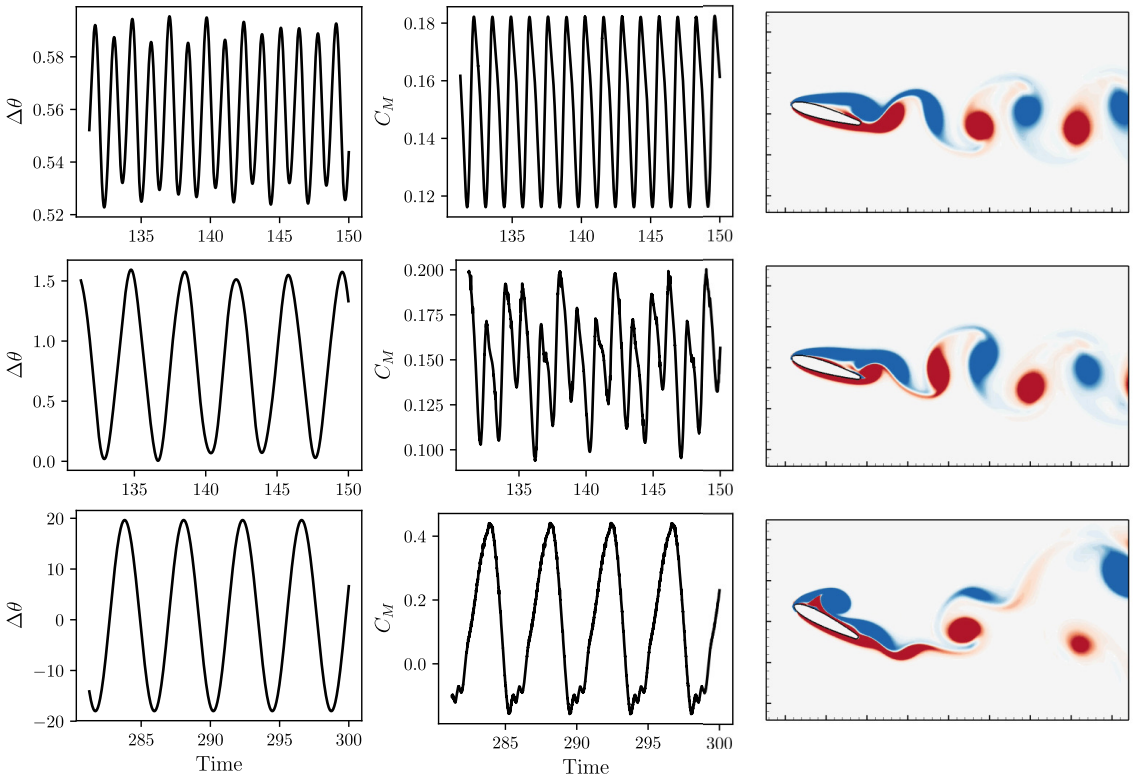

FIGURE 5. Pitch amplitude timeseries, ($\Delta\theta$), coefficient of moment (C_M), and a snapshot of vorticity contours for three regimes of response close to U_c^*; (top panel) $U^* = 3.3$; (middle panel) $U^* = 4.0$; (bottom panel) $U^* = 4.6$

to the pre-onset regime, we see that the response amplitude is very small ($A_\theta < 1°$), the frequency is high, and the pitch moment oscillates at a similar high frequency. Due to the small amplitude of oscillation, it makes sense to compare this with the behaviour of a static airfoil and we see that the response frequency is in fact very close to the vortex shedding frequency of a static airfoil at $\theta_0 = 15°$ ($f^* = 0.71$; see timeseries in figure 6). From the flow field it is clear that this regime corresponds to a Karman vortex shedding mode, much like the wake due to separated slow around a stationary bluff body. In fact, the dimensionless frequency in this regime, when calculated using the projected frontal length as the length scale, is $f^* \approx 0.17$, which is very close to the frequency of Karman shedding in bluff body wakes. In this regime, the coupling between the flow and airfoil pitching is effectively one-way, with the vortex shedding driving the pitching, but the pitching having virtually no effect on the vortex shedding.

In contrast, the flow field for $U^* = 4.6$, which corresponds to the post-bifurcation regime where the pitch response occurs at the natural frequency of the system, shows a very different character with the presence of a strong dynamic stall vortex generated at the leading edge. This is also apparent in the time-series of the moment coefficient, where the peak of the oscillation is accompanied by an abrupt drop in forcing. This drop in forcing has been observed by numerous studies as a hallmark of dynamic stall. In this regime, large (20°) amplitude pitch oscillations occur at the natural frequency, which in turn forces the generation and shedding of the stall vortex to occur at this frequency.

For the intermediate case of $U^* = 4.0$, which corresponds to the regime close to the bifurcation, the pitch time series shows low-frequency oscillations at to the natural frequency. The moment time series however seems to have frequency components corre-

sponding to the vortex shedding as well airfoil pitching time-scale. This is qualitatively seen in the flow field too, where the wake has the appearance of a slightly undulating or distorted Karman wake. Hence this is a transitional regime that occurs between the pre- and post-bifurcation regimes.

This regime of oscillation in fact agrees well with the observation of Poirel *et al.* (2008) who investigated flutter oscillations in this range of amplitudes. They too observed low-frequency pitch oscillations which showed no signature of the high-frequency Karman shedding occurring in the wake. Further, this low-frequency content is absent in the pre-bifurcation (or static) regime forcing response. The triggering of low-frequency oscillations in the absence of low-frequency forcing suggests that the flutter is not a result of an external periodic forcing, and is in fact self-sustained.

3.4. *Critical Reduced Velocity*

An obvious and important question raised by Figure 3 is - why does the critical U^* depend on θ_0? U^* represents a ratio the time-scale of the pitch oscillation to a time-scale for the flow. With regard to the pitch-time-scale, it is clear from the previous subsection that in the post-critical regime, the time-scale for the pitch oscillations does coincide with with the natural time-scale of the elastic system. Turning next to the flow time-scale in U^* we note that in most studies (including the current), the time-scale for the flow is assumed to be the convective time-scale of the flow over the body, i.e. C/U_∞. However, a more appropriate flow time-scale is one that is associated with the mechanism that triggers the flutter instability. In the well-studied case of flow-induced vibrations of circular cylinders, it is known that the trigger for the cylinder vibrations is Karman vortex shedding (Williamson & Govardhan 2004). The appropriate time-scale for determining the onset of these vibrations is therefore the vortex shedding time-scale (T_v), which is roughly about $5D/U_\infty$. Thus, a reformulation of the reduced velocity as the ratio of the natural time-scale of the elastic structure and the vortex shedding time-scale as $U_v^* = (1/f_s)/(5D/U_\infty)$ leads to the condition that vibrations are initiated when U_v^* approaches and exceeds unity. The identification of a similar scaling for the airfoil flutter observed in the current study, is the focus of the rest of this section.

Since we are concerned here with the *onset* of flutter, flow past a static airfoil should provide insights regarding the triggering mechanism. With this in mind we perform a set of simulations of flow over static airfoils at $Re = 1000$ with the angle-of-attack set to θ_0 for each case. The system is held at this angle-of-attack and the flow proceeds through the transient to its final stationary state. In figure 6 we show time-series plots of the lift and moment generated by these cases and also the instantaneous contours of spanwise vorticity for each case. The lowest θ_0 exhibits weak vortex shedding beyond the near wake whereas the other two cases exhibit separation of the boundary layer from the suction surface of the airfoil as well as vortex shedding in the wake with a topology that is quite similar to Karman shedding. The frequency corresponding to this vortex shedding is $0.81U_\infty/C$ and $0.71U_\infty/C$ for $\theta_0 = 10^\circ$ and 15°, respectively. However, these are higher than the frequency corresponding to the system at the onset of flutter and can therefore not be the triggering mechanisms for post-onset flutter oscillations. In fact, the static $\theta_0 = 5^\circ$ case does not exhibit vortex shedding but still undergoes a bifurcation to large-scale flutter, further confirming that wake vortex shedding is not the trigger for the bifurcation. This agrees with the observations of Poirel *et al.* (2008).

Figure 6 however, suggests an alternative time-scale for the onset and sustenance of flutter, which manifests itself during the initial transient over the static airfoil. The initial transient in the current simulations represents the initial growth, development, and saturation of the vorticity layer over the two surfaces of the airfoil and this transient

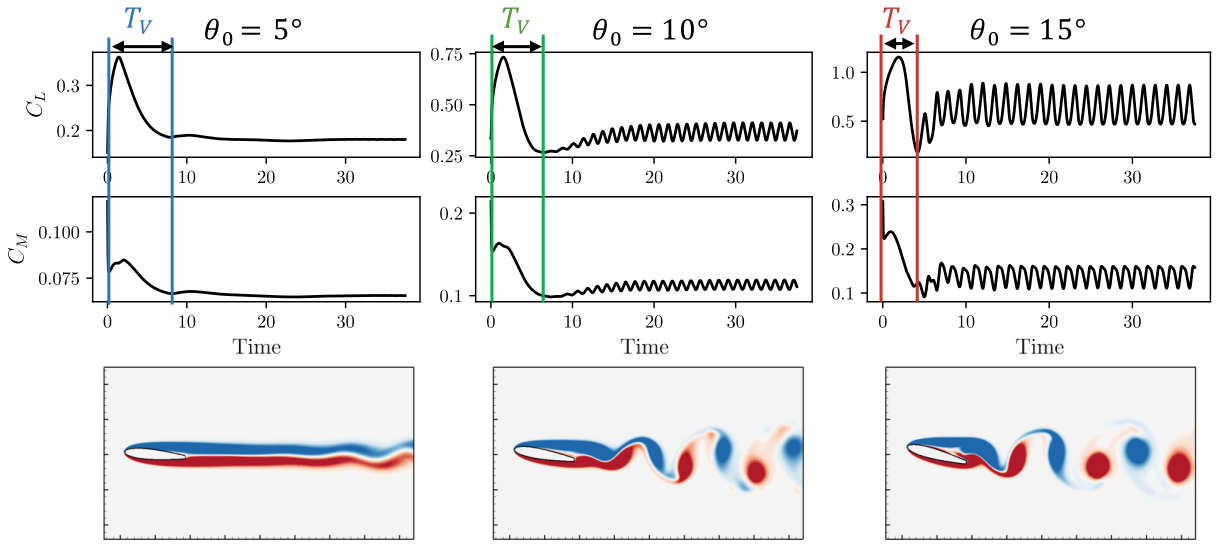

FIGURE 6. Time series of C_L and C_M for static airfoils at $\theta_0 = 5°, 10°, 15°$. The bottom panel shows an instantaneous snapshot of the flow after reaching stationary state for each case, coloured by vorticity contours. Also indicated is T_v, which represents the time-scale of the initial transient. Note: The flow snapshots do not show the entire computational domain, which extends roughly $5C$ beyond the edge of the figure.

is associated with a distinct, large-magnitude peak in the lift and moment, with a well-defined time-scale. This time-scale is associated with an intrinsic time-scale for the separated shear layer, which is the key driver for flutter. Based on this, we hypothesize that the time-scale that corresponds to the relaxation time of a perturbation in the separated shear layer would be the appropriate time-scale for determining the onset of flutter.

It is possible to estimate this time-scale for the current configuration by using a system-identification approach. This is done by providing a small perturbation to the angle-of-attack of an airfoil which is held stationary before and after the perturbation, and estimating the time it takes for the resulting pitching moment on the airfoil to relax back to the unperturbed state. In this study, the pitch perturbation takes the form $\theta_p(t) = A_p[1 - \cos\{2\pi(t - t_0)/\tau_p\}]$, where A_p is the amplitude of the perturbation, t_0 is the time at which the perturbation is applied, and τ_p is the duration of the perturbation. In the current case, τ_p is chosen equal to C/U_∞, which is much smaller than the observed timescales of the initial transient and resembles a "delta" perturbation. A qualitative representation of this perturbation is shown for the case of $\theta_0 = 5°$ in figure 7. We then compute the perturbation in the pitching moment by subtracting the unperturbed moment coefficient (which we refer to as C_{M_0}) from the pitching moment measured following the perturbation. For simplicity, these signals are filtered to remove vortex shedding oscillations. The required time-scale (T_v) is then estimated as the time taken by the energy of this perturbation to attain 5% of its peak value. The above procedure is performed for $\theta_0 = 5°, 10°, 15°$ using perturbations at various phases of the natural vortex shedding. Furthermore, the following magnitudes of perturbation, A_p are employed: $0.1°, 0.125°, 0.25°$ for $\theta_0 = 5°$; $0.125°, 0.25°, 0.5°$ for $\theta_0 = 10°$; and $1.5°, 2°, 2.5°$ for $\theta_0 = 15°$.

Figure 7 shows the time-variation in the moment coefficient for these various cases at each θ_0. It is observed that depending on the phase of vortex shedding at which the perturbation is applied, the perturbed moment coefficient can be positive or negative.

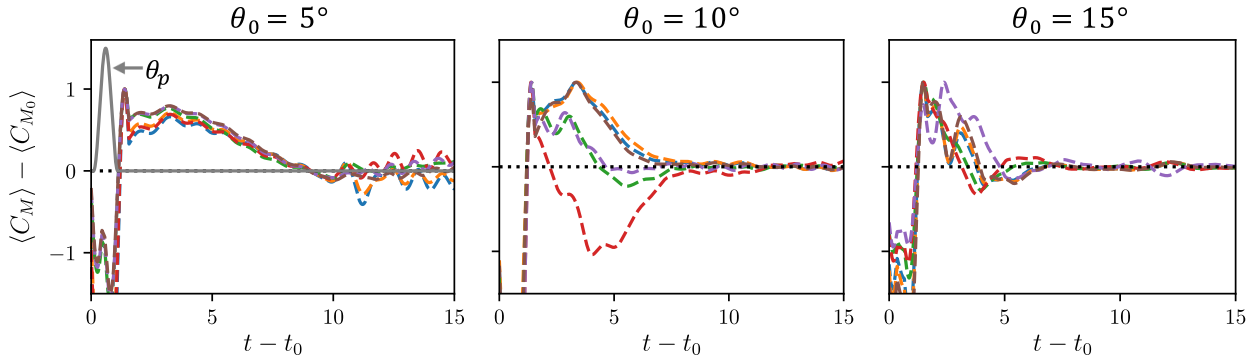

FIGURE 7. Relaxation of perturbed C_M as a result of small perturbations in angle of attack for static airfoils at $\theta_0 = 5°, 10°, 15°$ deg. $\langle C_M \rangle$ and $\langle C_{M_0} \rangle$ are filtered moment coefficients of perturbed and unperturbed cases respectively. The different curves in each plot correspond to different values of A_p and t_0. Also shown qualitatively for the case of $\theta_0 = 5°$ is the pitch angle perturbation, θ_p. Time in these plots is non-dimensionalized by C/U_∞.

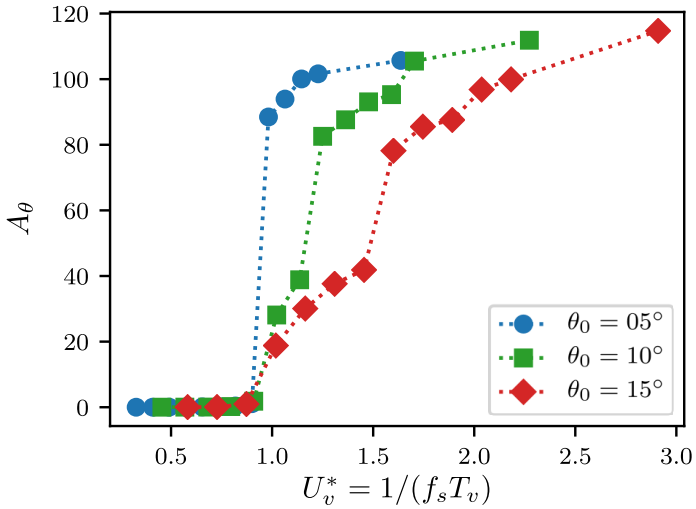

FIGURE 8. Maximum pitch deflection v/s $U_v^* = 1/(f_s T_v)$ for $\theta_0 = 5°, 10°, 15°$. Here $\zeta = 0.15$ and $X_e^* = 0.50$.

However, all the perturbation with different phases and magnitudes result in a consistent relaxation time-scale for each θ_0. This time-scale is estimated to be $T_v \approx 7.0$, 5.1 and 4.0 for $\theta_0 = 5°, 10°$ and $15°$, respectively. It is noted that the time-scale reduces with increasing angle-of-attack, a trend that was also observed for the initial transient in figure 6.

We now use T_v to define a new reduced velocity $U_v^* = 1/(f_s T_v)$. In figure 8 we replot the maximum pitch deflection (which was initially shown in Figure 3) v/s U_v^* and we find not only that the bifurcation points for the three cases collapse to nearly the same value, but also that this critical value is slightly above unity. This strongly suggests that T_v is the correct flow time-scale for this problem and in an analog of the flow-induced vibration of circular cylinder, $U_v^* \gtrapprox 1$ is the simple condition for the generation of large-scale flutter, at least for the low Reynolds numbers investigated here.

The $U_v^* \gtrapprox 1$ condition for flutter also provides a phenomenological basis for the onset of flutter. During the pre-bifurcation regime, where the structural stiffness is higher than the critical value, the natural time-scale is smaller than the flow time-scale. In this

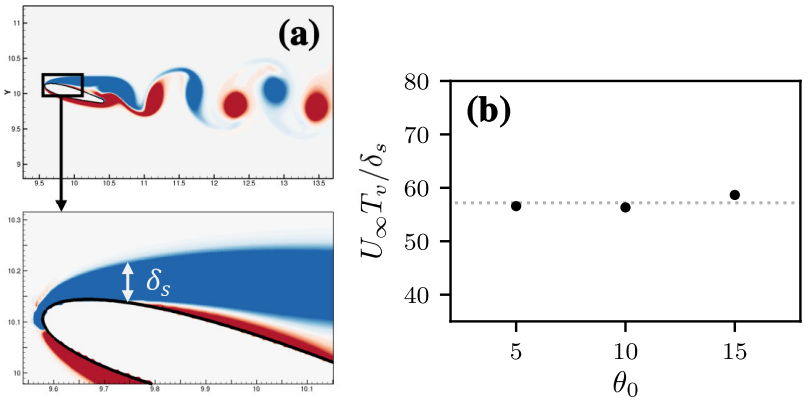

FIGURE 9. (a) Qualitative representation of boundary layer thickness at separation point for $\theta_0 = 15°$; (b) Scaling of the shear-layer timescale (T_v) with estimated boundary layer thickness (δ_s) for $\theta_0 = 5°, 10°, 15°$.

condition, the time-variation in pitching moment due to a perturbation in pitch does not have sufficient time to grow before the spring forces the airfoil back towards the equilibrium position. Thus, the interaction between the pitching motion and the pitching moment is not constructive and the system is not able to extract energy from the flow to sustain the oscillation. For $U_v^* > 1$, the natural time-scale exceeds the flow time-scale and the growth in the pitching moment associated with a pitch perturbation can now be accommodated by the spring. This constructive interaction between pitch and pitching moment is able to extract energy from the flow during a pitch perturbation, leading to growth of the pitch instability. In a later section, we will revisit this idea of energy extraction and its influence on driving aeroelastic flutter.

The physical underpinning of the dependence of T_v on the angle-of-attack is the final question regarding the onset of flutter. In particular, why does T_v decrease with increasing angle-of-attack? We base our analysis on the notion that T_v is related to the inherent instability of the shear layer that separates from the suction surface of the airfoil, and the natural time-scale of a shear layer that separates from a surface scales with the thickness of the shear layer at the point of separation. As the angle-of-attack is increased, the separation point moves upstream where the attached boundary layer is thinner, and therefore the shear layer thickness at the point of separation decreases with increasing angle-of-attack. We have estimated the boundary layer thickness (denoted by δ_s) at the point of separation for the static airfoil at the three angles-of-attack. This is shown qualitatively for $\theta_0 = 15°$ in figure 9(a). In figure 9(b) we plot the ratio of the shear layer timescale and boundary layer thickness, non-dimensionalized by U_∞ for the three angles-of-attack studied here. This dimensionless number represents a relaxation timescale associated with the shear layer and the plot indicates that δ_s and T_v have an approximately constant scaling with angle-of-attack. This supports our hypothesis that the reduction of T_v with angle-of-attack is related to the shear layer instability, which is in turn governed by its thickness at the point of separation.

3.5. *Structural damping and location of elastic axis*

In this section, we describe the effects of structural damping as well as the location of the elastic axis on flutter. In previous sections, we have described the response of the system with $b^* = 0.15b^*_{cr}$ and in this section, we compare these previous cases with the corresponding cases with zero damping. Further, we will make this comparison for two

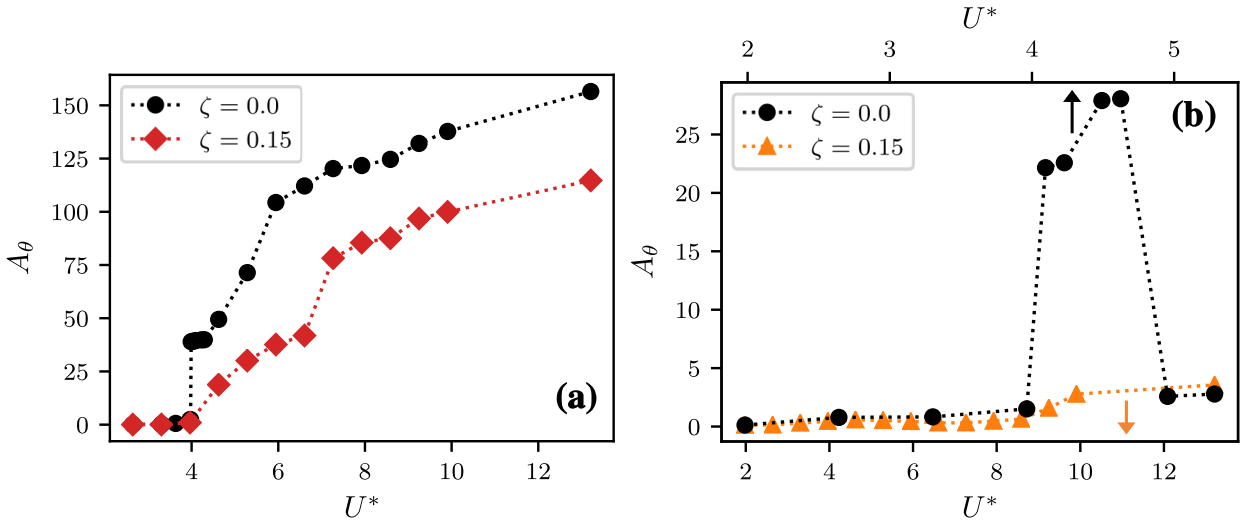

FIGURE 10. Effect of structural damping, ζ, on maximum pitch deflection for $\theta_0 = 15^\circ$. This is shown for two different locations of the elastic axis, (a) $X_e^* = 0.50$; (b) $X_e^* = 0.33$. Note: Range of U^* is different for each value of ζ in the case of $X_e^* = 0.33$.

different locations of the elastic axis: $X_e^* = 0.50$ and 0.33. The location of the elastic-axis with respect to the center-of-pressure is critical in determining the aeroelastic pitch stability of an airfoil. A center-of-pressure upstream of the elastic-axis leads to an unstable configuration that promotes the pitching instability, and vice-versa. In the context of pitching airfoils, there is the added consideration of the timing of leading-edge vortices convecting past the elastic axis. Each such vortex induces a pitching moment on the airfoil and the direction of this moment changes as the vortex convects past the elastic-axis. This could potentially lead to non-linear and non-monotonic behavior noted in 3.2.

In figures 10(a) and (b) we plot the maximum pitch deflection, A_θ, with and without structural damping, as a function of U^*, for two different locations of the elastic-axis and for $\theta_0 = 15^o$. For $X_e^* = 0.50$, we see that the overall trend of A_θ does not change significantly with damping. However, as expected, the undamped case shows a much larger amplitude of oscillations. We also see that the bifurcation to large amplitude oscillations is very abrupt for $\zeta^* = 0.0$, indicating a subcritical bifurcation. This agrees with the classical understanding of dynamical systems where the loss of a low-order damping term leads to a subcritical bifurcation (Strogatz 2018). However, the stabilizing influence of higher order non-linearities (from the flow, in this case) prevents the system from diverging, and hence causes limit-cycle oscillations.

As noted previously, the amplitude response for $X_e^* = 0.33$ exhibits significantly smaller oscillations, but a non-monotonic behaviour as the hinge location is moved upstream. Figure 10(b) shows that this non-monotonic behaviour of A_θ is much more apparent in the absence of structural damping, where we observe a very large and abrupt jump in flutter amplitude with U^*. However, further increase in U^* results in a large drop in the flutter amplitude. These types of non-monotonic responses have been studied extensively in flow-induced vibration of bluff bodies (Williamson & Govardhan 2008) but are quite unexplored for airfoil flutter.

Figure 11 shows the frequency response of the undamped system for $X_e^* = 0.50$ and 0.33 and it is clear that these cases show the same response regimes that were seen before - a high frequency Karman shedding mode, followed by oscillations at the natural frequency for increasing U^*. Further, this synchronization happens close to the critical U^*. Hence the frequency selection in this system follows a mechanism that is similar to

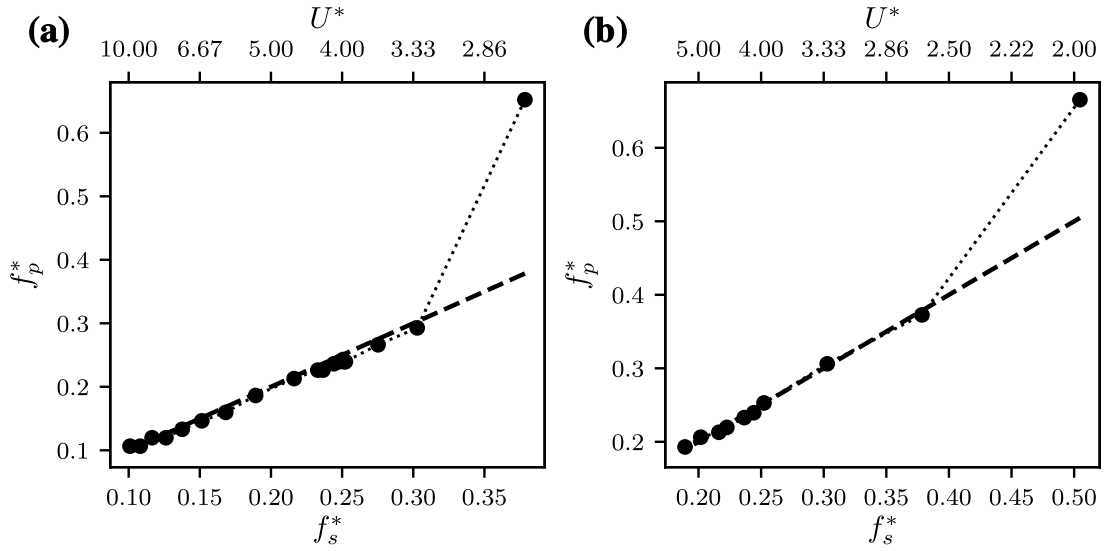

FIGURE 11. Pitching frequency response of undamped oscillations ($\zeta = 0.0$) for $\theta_0 = 15^\circ$ and two different locations of the elastic axis, (a) $X_e^* = 0.50$; (b) $X_e^* = 0.33$. The dashed line shows the natural frequency of the system.

that outlined previously, where the competition of time-scales determines the response frequency. However, the amplitude response warrants further investigation.

4. Flutter Analysis Based on Energy Maps

4.1. *Energy maps*

Our analysis in the preceding sections indicates a need to better understand the amplitude response of the flow-induced pitching airfoil for a set of given system parameters. We were able to demonstrate the mechanism governing the onset and frequency of oscillation as a competition of time-scales. However, the variations in amplitude with U^* and X_e^* are complex and non-intuitive. Here, we propose the use of "energy maps" to gain an understanding of the complex amplitude response of the system. For an airfoil undergoing sinusoidal pitching oscillations in a freestream, we can derive (see appendix A) the following equation for the growth of the amplitude over one cycle

$$A_\theta(t_n + T) - A_\theta(t_n) = \frac{E^*}{k^* \bar{A}_\theta} \tag{4.1}$$

where $\bar{A}_\theta$ is the average amplitude over a cycle. In the above equation $E^* = E_f^* - E_d^*$, where E_f^* is the energy extracted by the airfoil from the freestream over one oscillation cycle and E_d^* is the energy lost to structural damping. E_f^* is given by

$$E_f^* = \int_{t_n}^{t_n+T} C_M \dot{\theta} dt \tag{4.2}$$

where $\dot{\theta}$ is the angular velocity and T is the period of oscillation.

In the case of purely sinusoidal oscillations where $\dot{\theta} = \dot{\Theta}\sin(2\pi t/T)$ and $C_M = K\sin(2\pi t/T + \phi)$, the energy transfer is given by $E_f^* = (1/2)\,\dot{\Theta} K T \cos\phi$ and this simple model shows that the sign of energy extraction, which determines whether the airfoil extracts energy from the flow, is governed by the phase difference between the pitch velocity and the pitch moment. The physical interpretation of this phase difference, in the context of flow-induced oscillations, is related to the timing between the pitching

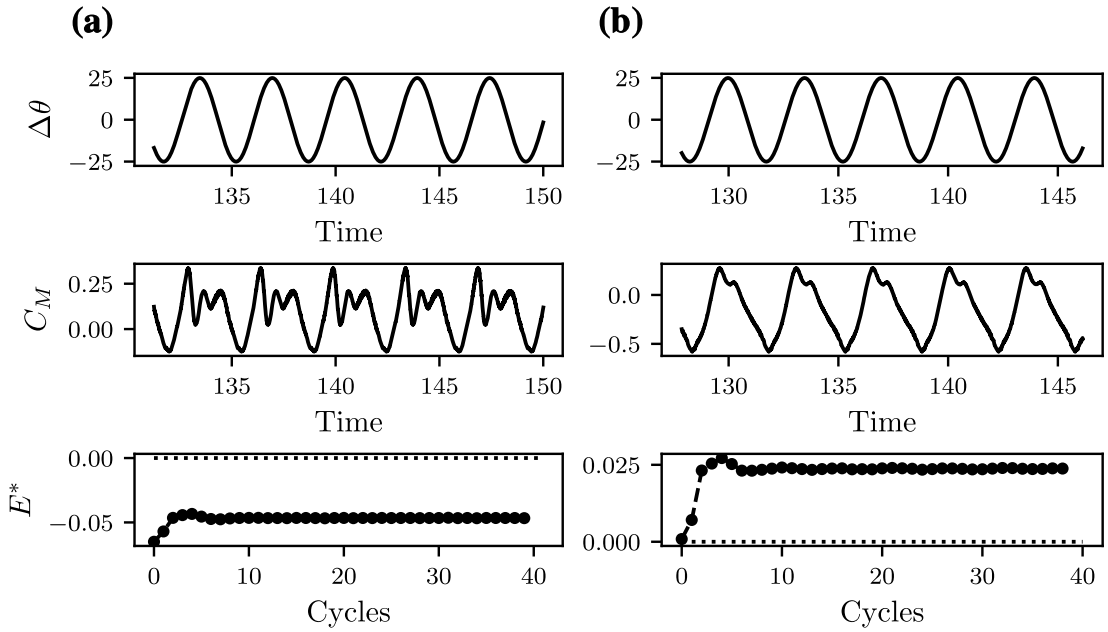

FIGURE 12. Comparison of $\Delta\theta$, C_M and extracted energy E_f^*, for airfoils forced to oscillate with $A_\theta = 25^\circ$ and $f_p^* = 0.25$ about two different hinge locations, (a) $X_e^* = 0.33$; (b) $X_e^* = 0.50$.

and the resulting response of the flow. In section 3.3, our description of the mechanism determining the frequency response showed that this timing determines the critical U^* for the bifurcation to large amplitude oscillations. The phase difference between pitch and pitch moment is also a strong factor when considering the changes in the location of the elastic axis. This is demonstrated in figure 12 where we show time series plots of the pitch deflection and moment coefficient for an airfoil forced to oscillate at $A_\theta = 25^\circ$, about two different locations of the elastic axis. These sample cases show that changing the elastic axis, while retaining the kinematics, produces very different forcing on the airfoil. This is a result of the timing associated with the shedding as well as convection of vortices past the hinge location. These effects were also demonstrated in figure 1. The difference in timing leads to the case with $X_e^* = 0.33$ being damped, while $X_e^* = 0.50$ extracts energy. These examples suggest that the phase difference, and hence energy extraction, is indeed an important factor in analyzing the response of flow-induced flutter.

The aim in this section is to use our knowledge of the energy extraction, as described above, to understand the amplitude response of the dynamical system as a function of the various parameters explored in this study. To do this, we first create a map of energy transfer as a function of the parameters of interest. This is done by performing simulations of airfoils that are forced to undergo sinusoidal pitching oscillations over a range of amplitudes and frequencies, while holding the other parameters such as X_e^* and Re fixed. The pitching and pitch-moment data from each of these simulations is then used to calculate the energy extracted by the airfoil. The validity of these energy maps, which are obtained from forced oscillations, for the case of free, flow-induced oscillations rests primarily on the assumption that the free oscillations are strictly sinusoidal. We find that this condition is indeed satisfied to a very large degree for all the cases simulated here (see figures 2 and 5) and a sinusoidal fit to the pitching time-series yields an R-square value of roughly 0.99 for nearly all cases studied. Indeed, energy maps have been used quite successfully to understand flow-induced vibration of bluff bodies (Morse &

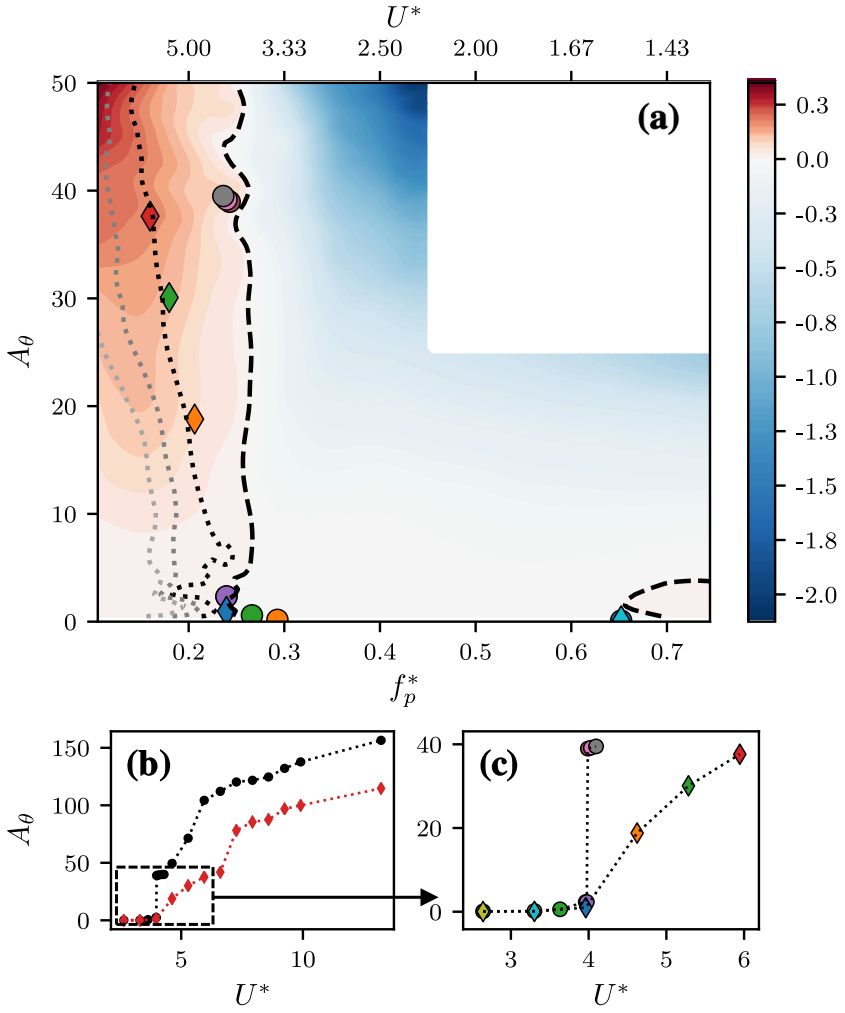

FIGURE 13. (a) Contours of energy extraction, E_f^*, as a function of oscillation amplitude and frequency for $X_e^* = 0.50$, $\theta_0 = 15°$. Symbols represent stationary state f_p^* and A_θ for undamped ($\circ$) and damped ($\diamond$) flow-induced oscillation cases. Dashed and dotted lines represent undamped ($E_f^* = 0$) and damped ($E_f^* = E_d^*$) equilibrium curves respectively. E_d^* is calculated using $\zeta = 0.15$ for the darkest damped equilibrium curve, and increasing values of ζ for subsequently lighter equilibrium curves ($\zeta = 0.30, 0.45$); (b) Reproduction of figure 10(a) with inset box showing range of U^* and A_θ computed in the energy map; (c) Zoom-in of flow-induced oscillation amplitudes for cases compared with the energy map.

Williamson 2009) and Bhat & Govardhan (2013) also demonstrated the use of an energy map to study flow-induced flutter of an airfoil.

The first map shown in figure 13 is for the case with $X_e^* = 0.50$ and $Re = 1000$. This map is the result of a total of ~ 300 simulations over a range of non-dimensional pitch frequencies $f_p^* = f_p C/U_\infty : [0.10, 0.75]$ and pitch amplitudes $A_\theta : [0, 50°]$. For each case, we simulate over 50 total cycles to ensure that a stationary state is achieved, and obtain E_f^* by integrating over the last 20 cycles. The dashed line in the energy map corresponds to $E_f^* = 0$ and the dotted line corresponds to $E_f^* = E_d^*$, where E_d^* is calculated using the value of structural damping previously specified in section 2.1. These represent potential equilibrium conditions in the case of flow-induced flutter.

The primary features in the map are the nearly vertical demarcation between regions of positive and negative energy transfer at about $f_p^* \approx 0.25$ and the small region of positive energy transfer around $f_p^* \approx 0.65$. From this energy map, we expect that sustained flow-

induced oscillations for cases with structural damping would occur in the region with $E_f^* > 0$, whereas cases without structural damping should saturate along the $E_f^* = 0$ contour line. To verify this, we superimpose on this map, the stationary-state amplitude and frequencies from the flow-induced flutter simulations for $X_e^* = 0.50$. We find that for all these cases, the system saturates very close to the contour line corresponding to net energy equilibrium, i.e., $E_f^* = 0$ for undamped oscillations and $E_f^* = E_d^*$ for damped oscillations. These observations provide clear confirmation of the validity of these energy maps as a tool for understanding the flow-induced flutter response.

Examining the energy maps further, we note that the nearly vertical $E_f^* = 0$ contour line lies very close to the frequency corresponding to the reciprocal of the critical velocity, which is the frequency at which the bifurcation to large amplitude oscillations occurs for the flow-induced oscillation with $X_e^* = 0.50$. This feature of the current energy map agrees qualitatively with that generated via experiments of Bhat & Govardhan (2013), despite the fact that their Reynolds number is an order-of-magnitude larger than the current one and their pitch axis is at quarter chord. Also, the small region of positive energy transfer on the right side of the map has a frequency that corresponds to the Karman oscillation mode identified earlier (see fig. 4).

The topology of the energy map and the equilibrium curve provide useful insights regarding the dynamics of this configuration. For instance, the nearly vertical demarcation between the regions of energy growth and decay at $f_p^* \approx 0.25$ suggests that an undamped system would experience rapid growth in flutter amplitude with a relatively small decrease (increase) in pitch frequency (reduced velocity). Indeed, figure 10(a) shows that the undamped system exhibits what seems to be a subcritical bifurcation at $U^* \approx 4.0$ with a jump in amplitude of nearly 40^o. As the structural damping is increased, the equilibrium curve bends to the left (i.e. increasingly negative slope) indicating a smoother onset of flutter. Furthermore, increased damping significantly limits the maximum amplitude attained by the system. Other implications of the topology of the energy map for the system dynamics are explored in the next section.

4.2. *Amplitude response for* $X_e^* = 0.33$

The case with $X_e^* = 0.33$ exhibits a very complex, non-monotonic response with U^* and we now demonstrate the utility of the energy maps in providing insight into this response. As shown in equation 4.1 and appendix A, oscillations in the absence of structural damping are expected to grow (decay) in regions of positive (negative) E_f^*. The requirements for a stable equilibrium are:

$$E_f^* = 0 \quad ; \quad dE_f^*/dA < 0 \tag{4.3}$$

Figure 14 shows the energy map for this case which is generated as before by conducting $\sim$ 200 simulations of prescribed flutter over a large range of pitch frequencies and amplitudes. On this energy map, we have identified the curves corresponding to the equilibrium condition ($E_f^* = 0$) as well as the regions of stability on these equilibrium curves ($dE_f^*/dA < 0$). A number of qualitative observations can immediately be made regarding this energy map. First, the topology is very different from that for $X_e^* = 0.50$. Since free oscillations can only exist within the region of $E_f^* \geqslant 0$, the energy map suggests an upper limit of $A_\theta \approx 40^\circ$ on the flow-induced oscillation amplitude in this case. The topology of the map is also extremely complicated: two main regions of energy growth and decay are separated by a complex equilibrium curve that extends over the entire range of frequencies considered here. There also exist multiple "islands" with $E_f^* < 0$ within the large region of energy growth in the low-amplitude ($< 10^\circ$) portion of the map, and

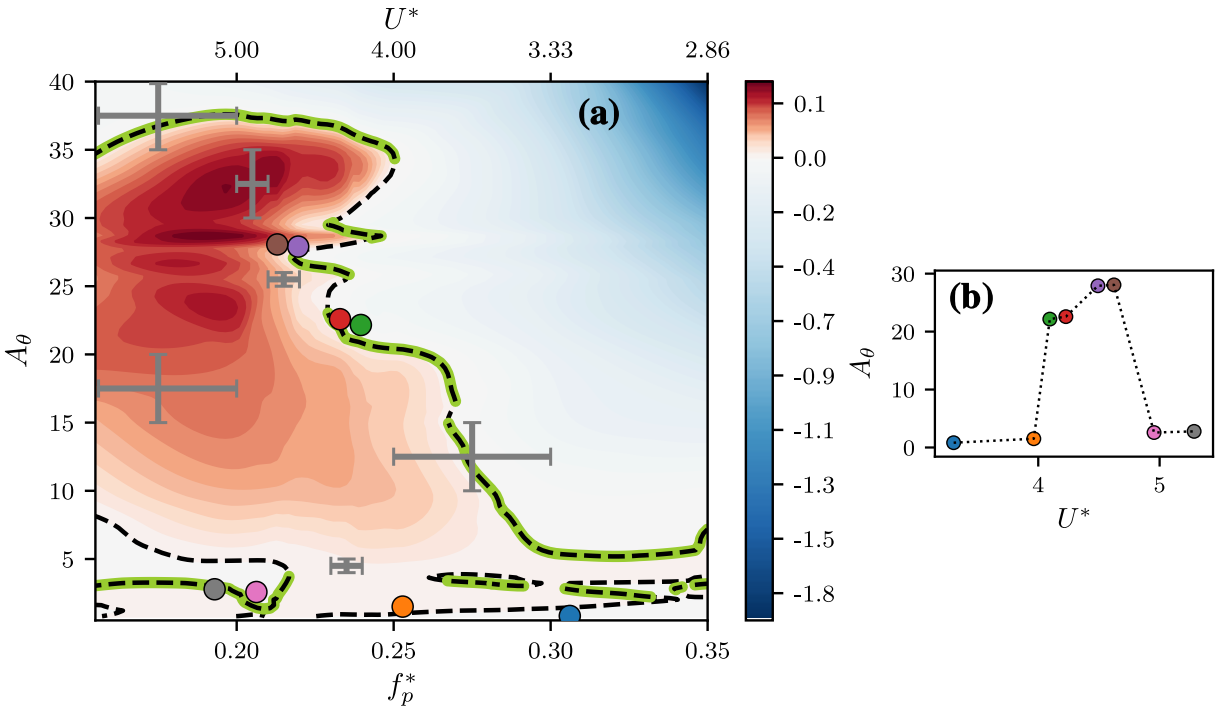

FIGURE 14. (a) Energy map for $X_e^* = 0.33$ and $\theta_0 = 15^\circ$, with the equilibrium curve ($E_f^* = 0$) shown as a dashed line, and stable equilibrium ($E_f^* = 0$, $dE^*/dA < 0$) highlighted along the equilibrium curve (thick line); (b) Maximum pitch deflections versus U^* for cases with $\zeta = 0$ corresponding to figure 10(b); The stationary state oscillation amplitude and frequency of all cases shown in (b) are plotted on the energy map using circles (○). Also shown on the energy map are bars indicating the local resolution in f_p^* and A_θ in various regions of the energy map. Local regions of the map that contain complex topological features have been provided higher resolution.

this points to the possibility of multiple equilibrium states for a given conditions as well as abrupt changes in oscillation amplitude with changes in the underlying parameters.

To compare our prediction for the equilibrium positions on this energy map, we superimpose the stationary state locations of our flow-induced data for $X_e^* = 0.33$ on the energy map using circle (○) symbols. This data set was described earlier in section 3.5 (see figure 10(b)) and is also shown as maximum pitch deflection versus U^* in figure 14(b). This data corresponds to zero structural damping, and is hence expected to lie along stable equilibria identified on the $E_f^* = 0$ curve. In figure 14 we see that there is again very good agreement between the flow-induced oscillations data and the energy map. The slight discrepancies in this comparison are a result of the finite resolution of the energy map, which is not able to fully resolve the complicated structure of the map. This is especially apparent at very small oscillation amplitudes, where multiple equilibria exist in close proximity to each other. Hence on figure 14 we have also plotted error-bars at various locations indicating the local step size in f_p^* and A_θ used in computing generating the energy map.

In spite of the difficulty in fully resolving the topology of the energy map, it allows us to explain the complex, non-monotonic response of the flow-induced flutter for the undamped $X_e^* = 0.33$ case. The map clearly shows that for $f_p^* > 0.25$ ($U^* < 4$) the system is trapped in a lower branch of the energy map which has very small amplitude. However, as f_p^* reduces below 0.25 ($U^* > 4$) the lower branch all but disappears. Thus for the case with $f_p^* > 0.237$ ($U^* = 4.22$) the system finds itself in a region of positive energy growth and the amplitude grows and saturates at the first stable equilibrium along the vertical

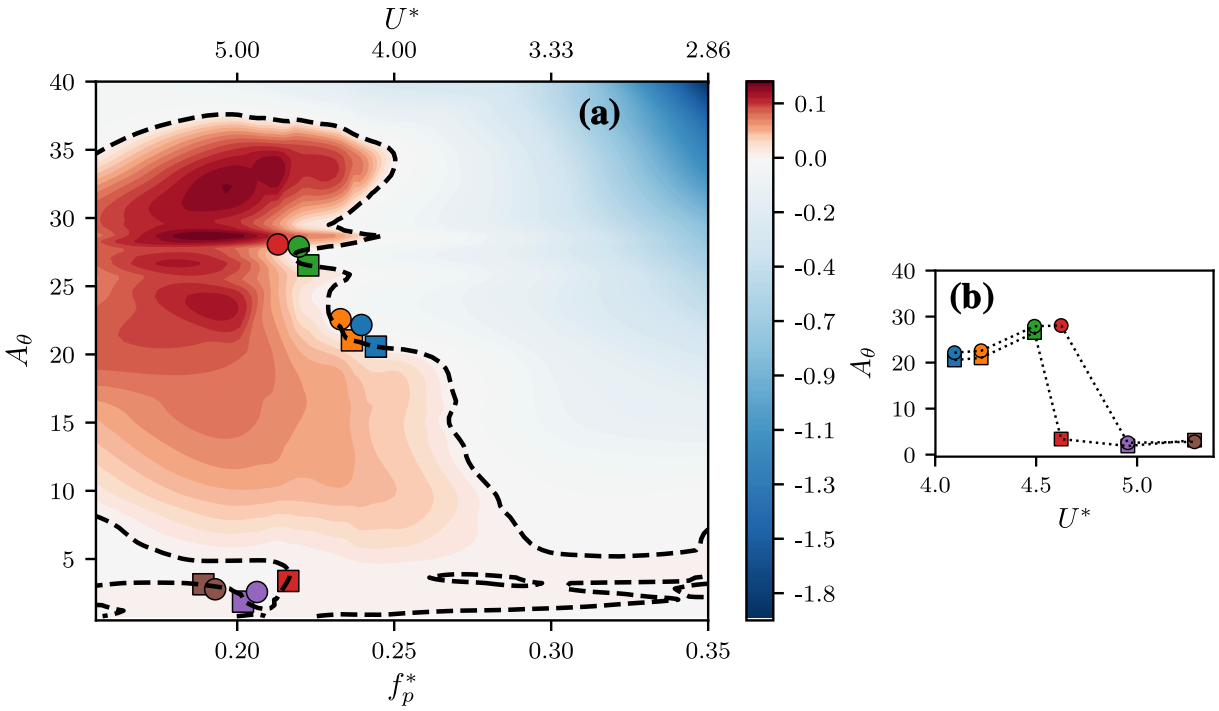

FIGURE 15. Prediction of A_θ using equation A 5, compared with calculations from flow-induced oscillation simulations. Here, $X_e^* = 0.33$ and $\theta_0 = 15°$; (a) Stationary state amplitudes and frequencies from the model (□), and flow-induced simulations corresponding to figure 14 (○) plotted on the energy map; (b) Corresponding amplitudes plotted against U^* using the same symbols as in (a).

line representing its natural frequency in the map, which is about $A_\theta = 22°$. Between $f_p^* = 0.22$ and 0.25, the system continues to grow to the large amplitudes associated with the upper equilibrium curve, however, for $f_p^* < 0.22$ ($U^* > 4.5$), a lower, stable equilibrium branch appears and the system locks on this lower branch. Hence, after the bifurcation to large amplitude oscillations at about $U^* = 4$, the amplitude of the system drops significantly ($\approx 3°$ for $U^* > 4.54$. In contrast, for the case of $X_e^* = 0.50$, there is no such lower branch in the energy map (see figure 13). Hence the oscillation amplitude increases monotonically along the $E_f^* = 0$ curve for that case.

Having established that the energy map indeed describes the stationary states of the flow-induced flutter system, we now demonstrate its use in making apriori predictions of the stationary state amplitude without the need for flow simulations. This serves as a demonstration of the energy map as a predictive tool as well as a validation of our model for amplitude growth (shown in the appendix). From equation A 5, we can calculate the amplitude growth of an oscillator at every cycle, with the knowledge of its spring stiffness and cycle-wise energy extraction. As mentioned before, this assumes that the oscillations are purely sinusoidal and occur at the natural frequency of the system. With these assumptions, we can pick the oscillation frequency of the system and predict the growth of amplitude based on the energy map and an initial condition. We iterate equation A 5 using a semi-implicit Crank-Nicholson scheme, and the iteration is performed until a stationary state is achieved. We demonstrate this for some selected cases in figure 15, where we compare the amplitude response observed in flow-induced oscillations (○), with that predicted by our model (□). We see that we are able to predict the amplitude response accurately for most cases by purely using the energy map. One case however, with $U^* = 4.62$, does not agree with the model's predictions. As is apparent

in figure 15(a), this is because the energy map computed here predicts the existence of a small amplitude stable equilibrium at this oscillation frequency. This is a result of finite resolution in computing the map, as was mentioned earlier. Furthermore, the fact that this region of the map is especially sensitive to small changes in frequency and amplitude amplifies the finite resolution effects. This sensitivity of the energy prediction to input conditions was also observed by Leontini *et al.* (2006).

4.3. *Transient Response*

The energy maps also allow us to understand the transient response of the various flow-induced flutter cases. In figure 16 we plot the pitching amplitude timeseries and trajectories of two cases of flow-induced flutter, where the circles represent the location of the oscillator on the frequency-amplitude space during each cycle. This is calculated by dividing the pitch response time series into individual cycles, and calculating the amplitude and timescale associated with each cycle. In the case of $U^* = 4.50$, we observe that the trajectory of the system follows a nearly vertical line on the energy map. This is because this case corresponds to the post-bifurcation regime, and the frequency is selected based on the natural frequency of the system. The system starts at rest, close to $\Delta\theta = 0$, and the amplitude grows due to the positive energy extracted from the flow. We see in figure 16(c) that this amplitude growth occurs until it reaches a stable equilibrium position corresponding to its oscillation frequency. However, before reaching this stationary state, the oscillator spends a long time close to a small amplitude equilibrium region, as shown by the density of circles in the zoomed-in trajectory shown in in figure 16(d). The effect of this is also seen in the pitch amplitude time series of this case, shown in figure 16(a). The system exhibits small amplitude oscillations for an extended period of time, before a sudden growth in amplitude caused by its escape from the small amplitude stable region.

On slightly increasing U^* to 4.95, the system to get trapped in the low-amplitude stable branch as seen in figure 16(c). Further, we see from the pitch response time series in figure 16(b) that the oscillation amplitude in this case shows an interesting beating behaviour. This suggests that the oscillator is trapped in a bi-stable region that allows it to move between two stable equilibrium positions. While the exact structure of this stable region is difficult to resolve, figure 16(d) shows that the system gets trapped in a nearly vertical branch of $E_f^* = 0$ that would allow the existence of multiple stable regions. Further, the vertical spread of instantaneous amplitudes after the system has reached a stationary state (shown by the spread of circles) suggests that the system does indeed move between two equilibrium states. The analysis of these cases shows the utility of the energy map in analyzing the stationary state response, as well as the trajectory of the oscillator from the initial condition to the stationary state. We also see that the complicated structure of the energy map leads to interesting behaviour in the pitching response of this system, which would be very difficult to interpret without knowledge of the corresponding energy map.

The energy map also allows us to predict hysteretic behaviour due to the presence of multiple stable equilibria at particular oscillation frequencies. In figure 17 we show the energy map, as in figure 14, with additional cases that demonstrate hysteresis shown using diamond ($\diamond$) symbols. These simulations were carried out using a previously computed stationary state along the equilibrium curve as an initial condition, changing the value of U^*, and allowing the dynamics to evolve to a new stationary state. We use arrows pointing from the initial to the final stationary state to denote the change in U^* in figure 17. We see that these cases agree with the equilibrium and stability conditions predicted by the energy map too.

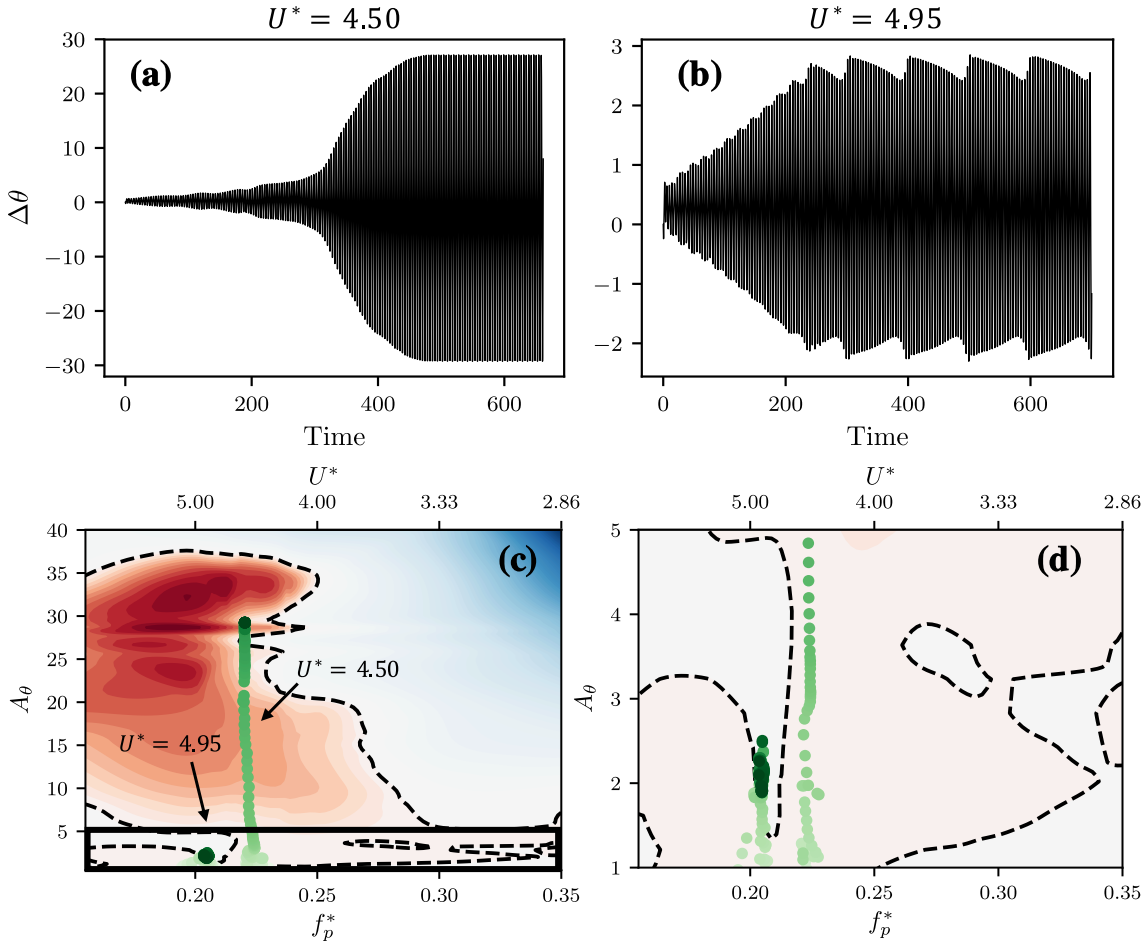

FIGURE 16. Comparison of two flow-induced oscillation cases with $U^* = 4.50$ and $U^* = 4.95$. Top panel shows timeseries of pitch oscillations for (a) $U^* = 4.50$, and (b) $U^* = 4.95$; (c) Amplitude-frequency trajectories of these cases on the energy map. Each circle represents the amplitude and frequency during one oscillation cycle. The colour intensity represents time; (d) Zoom-in of trajectories in the inset box shown in (c).

The transient response of these cases is especially interesting to analyze as they also demonstrate the ability to use these energy maps in flutter amplitude control. In figure 18 we plot the pitching time series and trajectories of two such cases showing hysteretic behaviour with $U^* = 3.30$ and $U^* = 4.95$. Figures 18(a) and 18(b) show timeseries plots of pitching amplitude, where the grey portion represents the last few cycles of the case used as an initial condition, and the black timeseries shows the subsequent amplitude response leading to the new stationary state. In figures 18(c) and 18(d) we show the trajectories of these cases where the circles show the state of the system on the frequency-amplitude space during each oscillation cycle. Here we show the trajectory leading up to the stationary state that is used as an initial condition, as well as the trajectory from the previous stationary state to the new one. The change in U^* is indicated by the arrow.

For $U^* = 3.30$, the case using the static initial condition shows very small amplitude oscillations ($A_\theta < 1°$) as seen in figure 10(b) and is described by the pre-bifurcation regime on section 3.3. However, when initialized with an oscillation amplitude $\sim 25°$, we see that it reaches a stationary state amplitude of roughly 10°. This new stationary state is achieved through a loss of energy, which is different from all the cases analyzed in this paper so far. The loss of energy is a consequence of the fact that the initial amplitude of oscillation, which corresponds to a stable equilibrium at a different natural frequency, is in

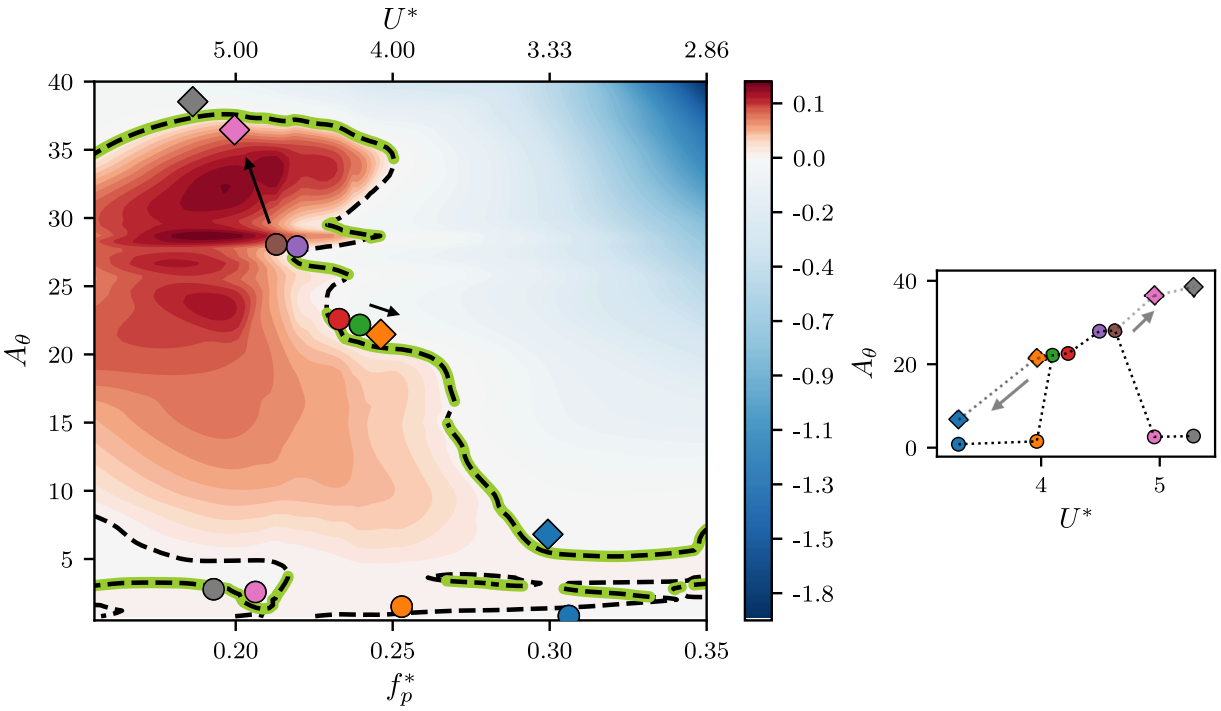

FIGURE 17. (a) Energy map for $X_e^* = 0.33$, with equilibrium curve, stable equilibria, and stationary state frequency and amplitudes as in figure 14. Also shown are cases demonstrating hysteresis, represented by diamonds (◇), by continuing along the directions indicated by the arrows; (b) The stationary state oscillation amplitude of all cases shown in the energy map, plotted against U^* using the same symbols.

a region of negative energy transfer at the natural frequency corresponding to $U^* = 3.30$. This results in a reduction in amplitude of oscillation as described by equation A 6, until it reaches a new stable equilibrium. This is an example of the ability to reduce the amplitude of flutter using a knowledge of the energy map.

The case of $U^* = 4.95$ shows a case that is initialized using a stationary state on one portion of the equilibrium curve, and ends up on higher-amplitude portion of the curve on changing its natural frequency. This occurs as the change in natural frequency pushes the system into a region of positive energy transfer, as indicated by the arrow in figure 18(d). Due to continuous extraction of energy from the flow, the amplitude grows until it reaches a new stable equilibrium. It must be noted that this is the same U^* value shown in the right-side pane of figure 16, where the static initial condition was used.

With these above examples we have been able to demonstrate the use of the idea of an energy map to analyze the dynamics of the flow-induced oscillator apriori, based on our knowledge of the frequency selection mechanism. We have also been able to explain the bizarre non-monotonic amplitude response seen in the case of $X_e^* = 0.33$ using this tool.

5. Conclusions

We have carried out a study of flow-induced airfoil flutter at a chord-based Reynolds number of 1000 using high-fidelity modelling of the fluid dynamics coupled with a linear structural model for deflection in pitch. The objectives of this work were two-fold - to carry out a systematic study of the parameters affecting the dynamics of wing flutter, and to demonstrate the use of the energy exchange between the fluid and the structure

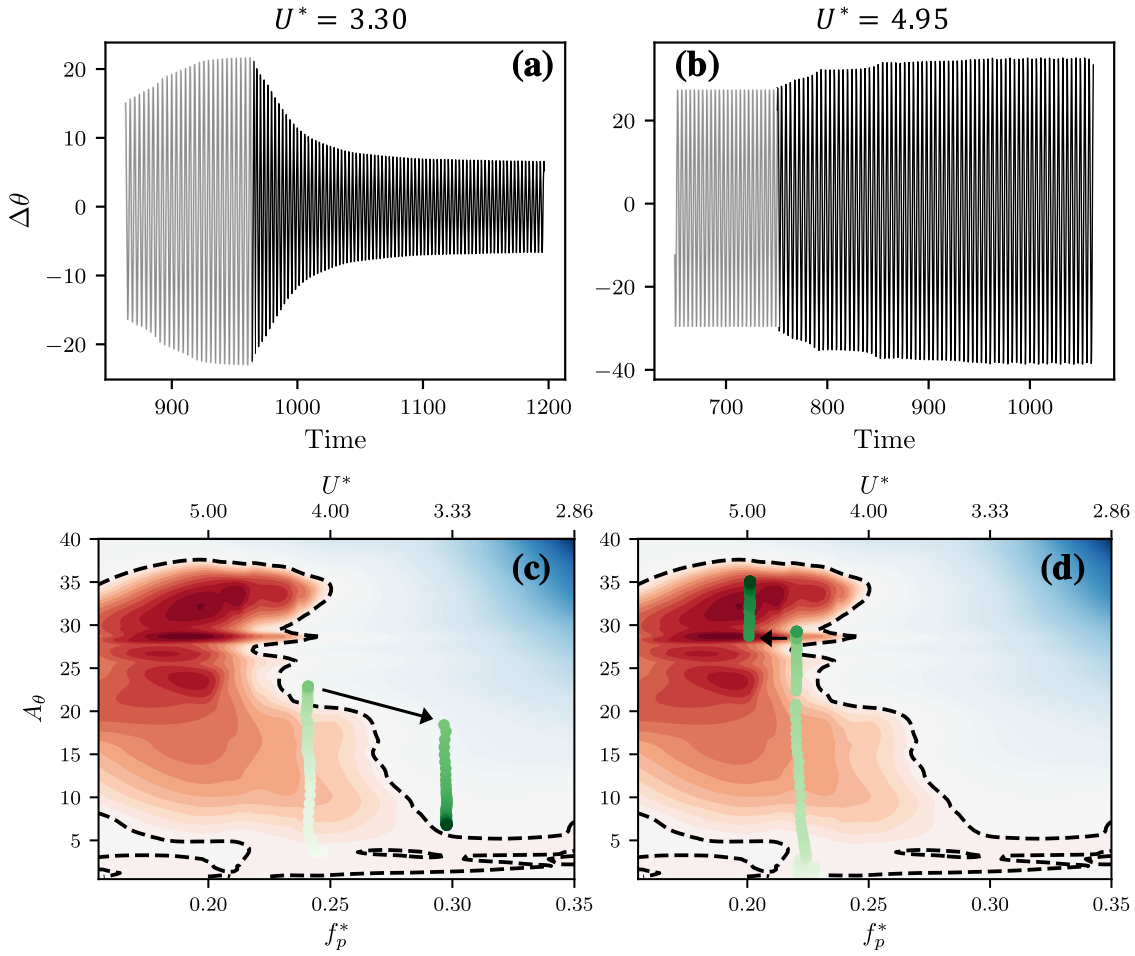

FIGURE 18. Trajectories of flow-induced oscillation cases showing hysteresis. Top panel shows timeseries of pitch oscillations for (a) $U^* = 3.30$, and (b) $U^* = 4.95$, where the lighter timeseries represents the approach to the initial state (before hysteresis) and the darker timeseries shows the evolution after the change of U^*; (c) Amplitude-frequency trajectories of the case with $U^* = 3.30$ on the energy map, where the approach to the initial condition as well as the subsequent evolution at $U^* = 3.30$ is shown; (d) Amplitude-frequency trajectories of the case with $U^* = 4.95$.

as a way to analyze the flutter behavior and its dependence on various parameters such as spring stiffness, elastic axis location and mean angle-of-attack.

It is shown that for cases that exhibit significant flutter, the onset of flutter occurs at a reduced velocity ($U^* = U_\infty/Cf_s$) which is dependent on the initial angle-of-attack. Simulations are used to determine a time-scale (T_v) corresponding to the relaxation of a pitch perturbation, which provides a more appropriate flow time-scale for this problem. A reduced velocity defined based on this time-scale, i.e. $U_v^* = f_s^{-1}/T_v$ leads to the simple condition that flutter will occur for $U_v^* > 1$, irrespective of the angle-of-attack. This condition provides a phenomenological basis for the onset of flutter: the natural time-scale of the system (f_s^{-1}) should be larger than the time-scale (T_v) of the flow so as to enable constructive coupling between the flow and the structure and amplification of a pitch perturbation. Finally, we provide some evidence that the time-scale T_v is proportional to the thickness of the boundary layer at the point of separation over the suction surface of the static airfoil, thereby connecting this time-scale to the instrinsic instability of the separated shear layer.

In the second part of this study, we demonstrated the use of "energy maps", as an

analytical tool to analyze the complex flow-induced flutter response of the airfoil. Energy maps are generated by computing the rate of energy exchange between the airfoil and the flow for airfoils undergoing prescribed pitch flutter over a range of amplitude and frequencies. The topology of the energy maps changes significantly with the location of the elastic-axis and we show that the energy maps provide a very effective means for interpreting complex behavior such as non-monotonic saturation amplitudes, hysteresis, subcritical and supercritical bifurcations, and complex limit-cycle behavior. Furthermore, we show that a simple mathematical model based on the energy maps can even predict the saturation amplitude without the need for flow-induced flutter simulation.

The current study and analysis has a number of limitations. The simulations are two-dimensional, limited to low-Reynolds numbers and they do not inform about how flutter would be affected by the introduction of new time-scales and strong instrisic three-dimensional effects associated with higher Reynolds numbers. The current study also does not address structures with multiple intrinsic modes/frequencies of flutter. We believe that the current approach of generating energy maps would be equally valuable in such systems, however the dynamics would live in a higher-dimensional energy map than demonstrated here. In general, each additional mode would correspond to an added dimension on the energy map. However, for the specific case of plunge oscillations with small amplitude or frequency, the added dimension could possibly be modelled in a quasi-steady manner as an effective angle-of-attack or using the model of Theodorsen (1935). It is also worth noting that in coupled pitch-plunge systems, we expect the mechanism for the onset of the instability in each mode to be similar to that described in section 3.4, i.e., a competition between the natural timescale of the structure and the relaxation timescale of the forcing. However, it is possible that the growth of plunge instability could force the growth of pitch oscillations, and vice-versa, due to the presence of subcritical response branches, as seen in this study. Another limitation to note is that the energy maps can have highly complex topologies that may be difficult to resolve fully. This also raises the question as to what features of the flow determine the topology of the energy map? This question is related primarily to the vortex dynamics in this coupled system, and such questions are interesting directions for future research.

Acknowledgment

This work is supported by the Air Force Office of Scientific Research Grant Number FA 9550-16-1-0404, monitored by Dr. Gregg Abate. The development of the flow solver used here has benefited from NSF grant CBET-1511200.

Appendix A. Model for Amplitude Growth

In this section, we present a mathematical model for amplitude growth and equilibrium for the flow-induced flutter of the airfoil. Multiplication of $\dot{\theta}$ to equation 2.2 as follows

$$I^*\ddot{\theta}\dot{\theta} + k^*(\theta - \theta_0)\dot{\theta} = C_M\dot{\theta} - b^*\dot{\theta}\dot{\theta} \tag{A 1}$$

results in a simple energy balance describing the growth of energy in the oscillator:

$$\implies \frac{d}{dt}\left(\frac{1}{2}I^*\dot{\theta}^2\right) + \frac{d}{dt}\left(\frac{1}{2}k^*\theta^2\right) = \frac{de_f^*}{dt} - \frac{de_d^*}{dt} = \frac{de^*}{dt} \tag{A 2}$$

where e_f^* is the energy extracted by the airfoil from the flow and e_b^* is the energy lost to structural damping. Integrating this equation over an oscillation cycle with time period

T, where the beginning of the cycle is at time t_n, results in an equation for the change of amplitude over the oscillation cycle.

$$I^*[\dot{\theta}^2(t_n+T)-\dot{\theta}^2(t_n)]+k^*[\theta^2(t_n+T)-\theta^2(t_n)]=2\left[e^*(t_n+T)-e^*(t_n)\right)]=2E^*. \quad (A\,3)$$

where E^* is the net energy gain of the structure over one cycle. Assuming a purely sinusoidal form for θ and $\dot{\theta}$, i.e. $\theta = A_\theta \sin\omega t$ where $\omega^* = 2\pi/T$, results in the following equation for the change in amplitude over an oscillation cycle

$$A_\theta^2(t_n+T)-A_\theta^2(t_n)=\frac{2E^*}{I^*\omega^2\cos^2\omega t+k^*\sin^2\omega t} \quad (A\,4)$$

Assuming the oscillation occur at the natural structural frequency, i.e., $\omega=\sqrt{k^*/I^*}$, we obtain the following equation for amplitude growth in the regime of oscillation at the natural frequency:

$$A_\theta^2(t_n+T)-A_\theta^2(t_n)=\frac{2E^*}{k^*} \quad (A\,5)$$

$$\implies A_\theta(t_n+T)-A_\theta(t_n)=\frac{E^*}{k^*\bar{A}_\theta} \quad (A\,6)$$

where $\bar{A}_\theta = [A_\theta(t_n+T)+A_\theta(t_n)]/2$.

This is the Poincaré map of this dynamical system. Equilibrium is attained when $A_\theta(t_n+T)=A_\theta(t_n)$, and this corresponds to

$$E^*=0 \quad (A\,7)$$

The equilibrium may be stable or unstable, and equation A 6 also allows us to derive a linearized stability condition for this system. For a system of the form $A_{n+1}=\mathcal{F}(A_n)$, where n is the index of the return map, and $\mathcal{F}$ is some functional form, linear stability requires $d\mathcal{F}/dA<1$ (Strogatz 2018). For our system, this gives the following condition for stability

$$\frac{d}{dA_\theta}\left(A_\theta+\frac{E^*}{k^*\bar{A}_\theta}\right)<1 \implies \frac{dE^*}{dA_\theta}<0 \quad (A\,8)$$

Thus, the above indicates that a system allowed to flutter freely will equilibrate only when conditions A 7 and A 8 are satisfied simultaneously. Thus, a map of E^* as a function of pitch frequency and amplitude could be used to understand, and even predict the response of the system. We note that this concept has previously been employed by other groups, primarily in the context of bluff body vibrations (Morse & Williamson 2009; Kumar *et al.* 2016). Furthermore, the equilibrium conditions arrived at here are the same as those employed in these previous studies.

Appendix B. Grid convergence and code validation

A grid convergence study was performed using forced oscillations of the truncated NACA0015 airfoil used in this study. The oscillations were performed about $\theta_0 = 20°$, with amplitude $A_\theta = 20°$ and frequency $f_p^* = 0.15$. The baseline grid tested consisted of 384×320 grid cells. This corresponds to a resolution of approx. 125 cells along the chord of the airfoil. This grid was compared to those with 480×448 and 544×544 grid cells, which correspond to 192 and 237 cells along the chord, respectively. These refined grids are 2.3× , and 3.6× the size of the baseline grid, in terms of total grid cells. In figure B.1 we show comparisons of the time-series of lift coefficient and moment coefficient for these three grids. The mean and RMS lift coefficient differ by 3.92% and 1.2% respectively between the baseline and 2.3× grid, and 0.96% and 1.51% respectively

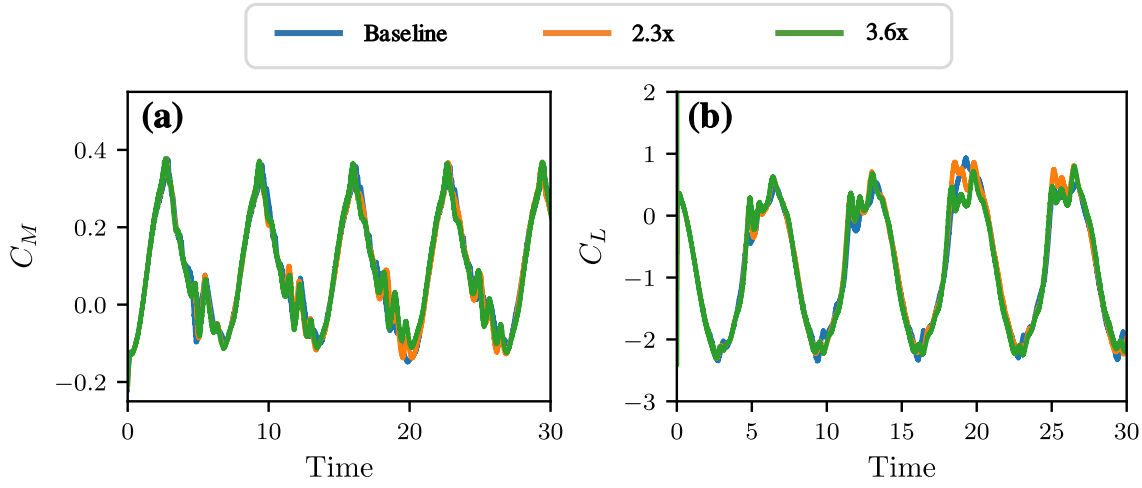

FIGURE B.1. Time series of (a) moment, and (b) lift coefficients, for the three grids tested.

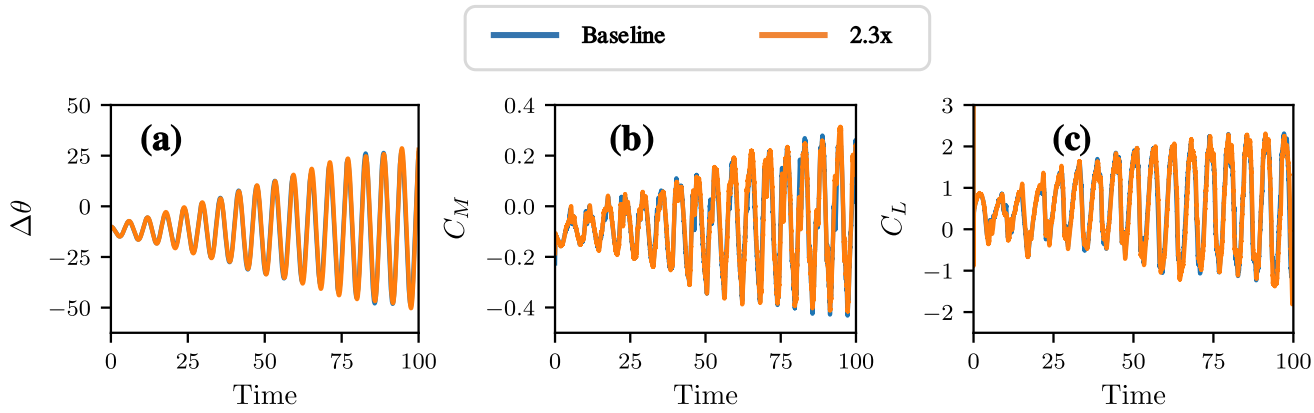

FIGURE B.2. Time series of (a) pitch angle; (b) moment coefficient; and (c) lift coefficients, for flow-induced oscillations at $U^* = 6.8$ using the Baseline and 2.3× grids.

between the baseline and 3.6× grid. The corresponding difference in mean and RMS moment coefficient is 1.78% and 1.07% between the baseline and 2.3× grid, and 0.84% and 2.05% between the baseline and 3.6× grid.

The grid convergence demonstrated above, while performed for forced oscillations, is expected to be a reasonably good demonstration of grid convergence for the flow-induced system as well. This is due to the fact that the only term in the dynamical equation for the solid (equation 2.2) that depends on the grid is C_M, which we have shown, is well converged. Further, in order to obtain statistics at a stationary state for the flow-induced system, CFL criterion-related constraints would require simulations with as many as 2,000,000 time-steps on the finer grids. This makes such an exercise computationally cost-prohibitive. However, in order to strengthen this demonstration of our grid convergence, we have performed a comparison of the baseline and 2.3× grid for a flow-induced oscillation simulation during the transient, amplitude-growth phase at $U^* = 6.8$ and $\theta_0 = 15°$. Plots for the pitch angle, and coefficients of moment and lift versus time are shown in figure B.2. We see that the mean and RMS lift coefficient differ by 0.57% and 1.56% respectively. The mean and RMS moment coeff. differ by 3.78% and 1.22% respectively. The maximum pitching amplitude differs by 6.44%.

Further, we have made various comparisons of results from the code used in this work with previous studies, in addition to the validation already mentioned in Mittal *et al.*

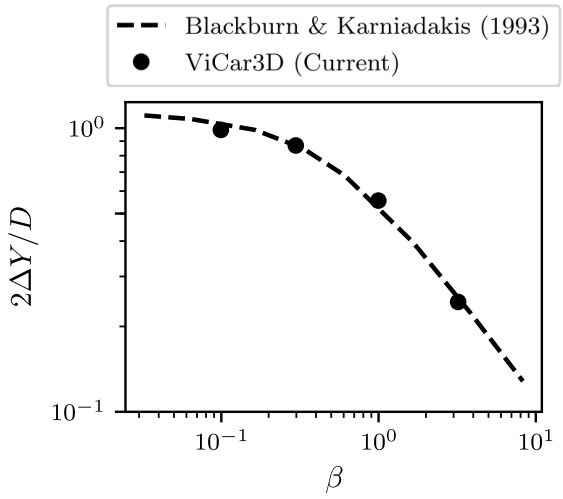

FIGURE B.3. Flow-induced oscillation amplitude of a circular cylinder versus mass-damping parameter $\beta = 8\pi^2 St^2 m\zeta/\rho D^2$. Results from the present code are shown using symbols and are compared with results from Blackburn & Karniadakis (1993) shown as a dashed line.

(2008). Specifically, force coefficients as well as Strouhal numbers predicted by ViCar3D for flow over static airfoils match very well with existing literature. These results are not shown here for the sake of brevity. In order to validate our fluid-structure interaction solver, we have performed simulations of flow-induced vibration of circular cylinders and compared our amplitude response with the results of Blackburn & Karniadakis (1993). In figure B.3 we show the amplitude response of a freely vibrating cylinder at $Re_D = 200$ with $m^* = m/\rho D^2 = 10$, against the mass-damping parameter $\beta = 8\pi^2 St^2 m\zeta/\rho D^2$. Here, St, m, ζ, ρ, and D are the vortex shedding Strouhal number, mass, damping ratio, fluid density, and cylinder diameter respectively. The symbols show results from our simulations and the dashed line is from the work of Blackburn & Karniadakis (1993). The agreement is quite reasonable.

REFERENCES

ABBOTT, I. H. & VON DOENHOFF, A. E. 1959 *Theory of wing sections, including a summary of airfoil data*. Courier Corporation.

AKBARI, M. H. & PRICE, S. J. 2003 Simulation of dynamic stall for a NACA 0012 airfoil using a vortex method. *Journal of Fluids and Structures* **17** (6), 855–874.

AMIRALAEI, M. R., ALIGHANBARI, H. & HASHEMI, S. M. 2010 An investigation into the effects of unsteady parameters on the aerodynamics of a low Reynolds number pitching airfoil. *Journal of Fluids and Structures* **26** (6), 979–993.

ARGENTINA, M. & MAHADEVAN, L. 2005 Fluid-flow-induced flutter of a flag. *Tech. Rep.* 6.

ASHRAF, M. A., YOUNG, J. & LAI, J. C.S. 2011 Reynolds number, thickness and camber effects on flapping airfoil propulsion. *Journal of Fluids and Structures* **27** (2), 145–160.

BHAT, S. S. & GOVARDHAN, R. N. 2013 Stall flutter of NACA 0012 airfoil at low Reynolds numbers. *Journal of Fluids and Structures* **41**, 166–174.

BLACKBURN, H M & KARNIADAKIS, G E 1993 Two- and Three-Dimensional Simulations of Vortex-Induced Vibration of a Circular Cylinder. *3rd Int. Offshore & Polar Engng Conf., Singapore* (1977), 715–720.

BRUNTON, S. & ROWLEY, C. 2009 Modeling the unsteady aerodynamic forces on small-scale wings. In *47th AIAA Aerospace Sciences Meeting Including the New Horizons Forum and Aerospace Exposition*, p. 1127.

Dimitriadis, G. & Li, J. 2009 Bifurcation Behavior of Airfoil Undergoing Stall Flutter Oscillations in Low-Speed Wind Tunnel. *AIAA Journal* **47** (11), 2577–2596.

Dowell, E. H. 1966 Nonlinear Oscillations of a Fluttering Plate. *AIAA Journal* **4** (7), 1267–1275.

Dowell, E. H & Hall, K. C. 2001 Modeling of Fluid-Structure Interaction. *Annual Review of Fluid Mechanics* **33** (1), 445–490.

Ducoin, A. & Young, Y. L. 2013 Hydroelastic response and stability of a hydrofoil in viscous flow. *Journal of Fluids and Structures* **38**, 40–57.

Eldredge, J. D. & Jones, A. R. 2019 Leading-Edge Vortices: Mechanics and Modeling. *Annu. Rev. Fluid Mech* **51**, 75–104.

Ericsson, L. E. & Reding, J. P. 1988 Fluid mechanics of dynamic stall part I. Unsteady flow concepts. *Journal of Fluids and Structures* **2** (1), 1–33.

Gharali, K. & Johnson, D. A. 2013 Dynamic stall simulation of a pitching airfoil under unsteady freestream velocity. *Journal of Fluids and Structures* **42**, 228–244.

Ghias, R., Mittal, R. & Dong, H. 2007 A sharp interface immersed boundary method for compressible viscous flows. *Journal of Computational Physics* **225** (1), 528–553.

Hall, K. C. 1994 Eigenanalysis of Unsteady Flows About Airfoils, Cascades, and Wings. *AIAA Journal* **32** (12), 2426–2432.

Holmes, P. & Marsden, J. 1978 Bifurcation to divergence and flutter in flow-induced oscillations: an infinite dimensional analysis. *Automatica* **14** (4), 367–384.

Hover, F. S., Techet, A. H. & Triantafyllou, M. S. 1998 Forces on oscillating uniform and tapered cylinders in crossflow. *Journal of Fluid Mechanics* **363**, 97–114.

Jones, K. D. & Platzer, M. F. 1996 Time-domain analysis of low-speed airfoil flutter. *AIAA Journal* **34** (5), 1027–1033.

Jumper, E J, Dimmick, R L & Allaire, A J S 1989 The effect of pitch location on dynamic stall. *Journal of Fluids Engineering* **111** (3), 256–262.

Kumar, S., Navrose & Mittal, S. 2016 Lock-in in forced vibration of a circular cylinder. *Physics of Fluids* **28** (11).

Lee, T. & Gerontakos, P. 2004 Investigation of flow over an oscillating airfoil. *Journal of Fluid Mechanics* **512**, 313–341.

Leontini, J. S., Stewart, B. E., Thompson, M. C. & Hourigan, K. 2006 Predicting vortex-induced vibration from driven oscillation results. *Applied Mathematical Modelling* **30** (10), 1096–1102.

McCroskey, W J 1982 Unsteady Airfoils. *Ann. Rev. Fluid Mech* **14**, 285–311.

Mittal, R., Dong, H., Bozkurttas, M., Najjar, F. M., Vargas, A. & von Loebbecke, A. 2008 A versatile sharp interface immersed boundary method for incompressible flows with complex boundaries. *Journal of Computational Physics* **227** (10), 4825–4852.

Mittal, R. & Iaccarino, G. 2005 Immersed Boundary Methods. *Annual Review of Fluid Mechanics* **37** (1), 239–261.

Morse, T. L. & Williamson, C. H.K. 2009 Prediction of vortex-induced vibration response by employing controlled motion.

Morse, T. L. & Williamson, C. H K 2006 Employing controlled vibrations to predict fluid forces on a cylinder undergoing vortex-induced vibration. *Journal of Fluids and Structures* **22** (6-7), 877–884.

Mueller, T. J. & DeLaurier, J. D. 2003 Aerodynamics of Small Vehicles. *Annual Review of Fluid Mechanics* **35** (1), 89–111.

Olivieri, S., Boccalero, G., Mazzino, A. & Boragno, C. 2017 Fluttering conditions of an energy harvester for autonomous powering. *Renewable Energy* **105**, 530–538.

Onoue, K. & Breuer, K. S. 2016 Vortex formation and shedding from a cyber-physical pitching plate. *Journal of Fluid Mechanics* **793**, 229–247.

Onoue, K. & Breuer, K. S 2018 A scaling for vortex formation on swept and unswept pitching wings. *J. Fluid Mech* **832**, 697–720.

Onoue, K., Song, A., Strom, B. & Breuer, K. S. 2015 Large amplitude flow-induced oscillations and energy harvesting using a cyber-physical pitching plate. *Journal of Fluids and Structures* **55**, 262–275.

Orchini, A., Mazzino, A., Guerrero, J., Festa, R. & Boragno, C. 2013 Flapping states

of an elastically anchored plate in a uniform flow with applications to energy harvesting by fluid-structure interaction. *Physics of Fluids* **25** (9), 97105.

Patil, M. J. & Hodges, D. H. 2004 On the importance of aerodynamic and structural geometrical nonlinearities in aeroelastic behavior of high-aspect-ratio wings. *Journal of Fluids and Structures* **19** (7), 905–915.

Peng, Z. & Zhu, Q. 2009 Energy harvesting through flow-induced oscillations of a foil. *Physics of Fluids* **21** (12), 1–9.

Poirel, D., Harris, Y. & Benaissa, A. 2008 Self-sustained aeroelastic oscillations of a NACA0012 airfoil at low-to-moderate Reynolds numbers. *Journal of Fluids and Structures* **24** (5), 700–719.

Poirel, D., Métivier, V. & Dumas, G. 2011 Computational aeroelastic simulations of self-sustained pitch oscillations of a NACA0012 at transitional Reynolds numbers. *Journal of Fluids and Structures* **27** (8), 1262–1277.

Ramesh, K., Murua, J. & Gopalarathnam, A. 2015 Limit-cycle oscillations in unsteady flows dominated by intermittent leading-edge vortex shedding. *Journal of Fluids and Structures* **55**, 84–105.

Sarpkaya, T. 1978 Fluid forces on oscillating cylinders. *NASA STI/Recon Technical Report A* **78**, 275–290.

Seo, J. H. & Mittal, R. 2011 A sharp-interface immersed boundary method with improved mass conservation and reduced spurious pressure oscillations. *Journal of Computational Physics* **230** (19), 7347–7363.

Shyy, W., Lian, Y., Tang, J., Viieru, D. & Liu, H. 2007 *Aerodynamics of low Reynolds number flyers*, , vol. 22. Cambridge University Press.

Staubli, T. 1983 Calculation of the vibration of an elastically mounted Cylinder using experimental data From forced oscillation. *Journal of Fluids Engineering* **105** (2), 225.

Strogatz, S. H. 2018 *Nonlinear Dynamics and Chaos: With Applications to Physics, Biology, Chemistry, and Engineering*. CRC Press.

Theodorsen, T. 1935 General theory of aerodynamic instability and the mechanism of flutter naca report no. 496. *Tech. Rep.*. Langley: US National Advisory Committee for Aeronautics.

Williamson, C.H.K. & Govardhan, R. 2004 Vortex-Induced Vibrations. *Annual Review of Fluid Mechanics* **36** (1), 413–455.

Williamson, C. H K & Govardhan, R. 2008 A brief review of recent results in vortex-induced vibrations. *Journal of Wind Engineering and Industrial Aerodynamics* **96** (6-7), 713–735.

Young, J., Lai, J. C. S. & Platzer, M. F. 2014 A review of progress and challenges in flapping foil power generation. *Progress in Aerospace Sciences* **67**, 2–28.